Bulletin of the Seismological Society of America, Vol. 96, No. 6, pp. 2181–2205, December 2006, doi: 10.1785/0120050245

Ⓔ

Earthquake Ground-Motion Prediction Equations for Eastern North America

by Gail M. Atkinson and David M. Boore

Abstract New earthquake ground-motion relations for hard-rock and soil sites in eastern North America (ENA), including estimates of their aleatory uncertainty (variability) have been developed based on a stochastic finite-fault model. The model incorporates new information obtained from ENA seismographic data gathered over the past 10 years, including three-component broadband data that provide new information on ENA source and path effects. Our new prediction equations are similar to the previous ground-motion prediction equations of Atkinson and Boore (1995), which were based on a stochastic point-source model. The main difference is that high-frequency amplitudes ($f \geq 5$ Hz) are less than previously predicted (by about a factor of 1.6 within 100 km), because of a slightly lower average stress parameter (140 bars versus 180 bars) and a steeper near-source attenuation. At frequencies less than 5 Hz, the predicted ground motions from the new equations are generally within 25% of those predicted by Atkinson and Boore (1995). The prediction equations agree well with available ENA ground-motion data as evidenced by near-zero average residuals (within a factor of 1.2) for all frequencies, and the lack of any significant residual trends with distance. However, there is a tendency to positive residuals for moderate events at high frequencies in the distance range from 30 to 100 km (by as much as a factor of 2). This indicates epistemic uncertainty in the prediction model. The positive residuals for moderate events at <100 km could be eliminated by an increased stress parameter, at the cost of producing negative residuals in other magnitude-distance ranges; adjustment factors to the equations are provided that may be used to model this effect.

Online material: Database of response spectra for hard-rock sites in ENA.

Introduction

A decade has passed since Atkinson and Boore (1995) developed their ground-motion prediction equations for eastern North America (ENA). The Atkinson and Boore (1995) prediction equations (AB95) were based on a stochastic point-source methodology (Boore, 1983), with the model's source and attenuation parameters determined from empirical data from small to moderate earthquakes in ENA. Specifically, the AB95 model rested heavily on the two-corner source spectral model of Atkinson (1993a) and the spectral attenuation model of Atkinson and Mereu (1992).

Since 1995, there have been several advancements that make it timely to develop new ENA ground-motion prediction equations:

1. An additional 10 years of ground-motion data have been gathered, including broadband data that extend the bandwidth of ENA ground-motion databases (Atkinson, 2004) and improve the definition of attenuation trends within 100 km of the source.
2. New analyses demonstrate that attenuation in ENA in the first 70 km is faster than previously believed. The geometric spreading rate is $R^{-1.3}$, where R is hypocentral distance (Atkinson, 2004). The new attenuation has a significant impact on predicted ground motions.
3. Stochastic finite-fault modeling techniques that can be used to develop regional ground-motion prediction equations for both point sources and large faults have been extended and validated (Beresnev and Atkinson, 1997a, 1998b, 2002; Motazedian and Atkinson, 2005). It has also been demonstrated that a point-source model can mimic the salient effects of finite-fault models through appropriate specification of an equivalent point-source representation (Atkinson and Silva, 2000). As a result of developments in stochastic modeling, it is now feasible to use a finite-fault model to improve ground-motion predictions for larger earthquakes in ENA. The use of a finite-fault model is particularly important in improving the reliability of estimates for large-magnitude events at close distances, for which the point-source approximation is known to perform poorly.

This article presents new ENA ground-motion prediction equations for hard-rock sites based on a stochastic finite-fault model. Relations are also presented for a reference site condition of National Earthquake Hazards Reduction Program (NEHRP) B/C boundary (shear-wave velocity, 760 m/sec), and nonlinear amplification factors are presented that convert from B/C boundary to softer site conditions. The input parameters to the model are assigned based on current information on ENA source, path, and site effects as obtained from empirical studies of seismographic and strong-motion data in ENA. The effects of aleatory uncertainty in model parameters are included in the simulations. Epistemic uncertainty is partially modeled by examining the influence of epistemic uncertainty in stress parameter, which is the largest source of epistemic uncertainty. It is also evaluated through comparisons of the results of this study with other prediction equations. The stochastic finite-fault model predictions are compared with ENA ground-motion data, and with other ground-motion prediction equations, including the previous point-source predictions of Atkinson and Boore (1995). The model parameters were derived largely from data recorded on hard-rock sites (with shear-wave velocity $\geq$2 km/sec) in the northeastern United States and southeastern Canada. However, past studies (Electric Power Research Institute [EPRI], 1993) have shown that ground-motion relations are expected to be similar, for a given site condition, over a broad region of ENA including the midcontinent.

Methodology and Model Parameters

Ground-motion prediction equations are developed for response spectra (pseudo-acceleration, 5% damped), peak ground acceleration (PGA) and peak ground velocity (PGV), for hard-rock sites in ENA (near-surface shear-wave velocity $\beta \geq 2$ km/sec, or NEHRP site class A), as a function of moment magnitude and closest distance to the fault rupture. For seismic-hazard analysis, we are primarily interested in ground motions from earthquakes of moment magnitude (**M**) >5, at distances less than 100 km from the source. Because of the paucity of recorded ENA ground motions in this magnitude-distance range, it is not feasible to develop ENA ground-motion prediction equations directly from regression analysis of empirical data. Rather, ENA ground-motion prediction equations are derived from a simulated ground-motion database. The simulated ground motions are developed from a seismological model of source, path, and site parameters. For this study, the seismological model parameters are obtained using empirical data from small to moderate ENA earthquakes. The methodology itself has been validated by comparing data and predictions in datarich regions. Finally, the model predictions are compared with the available ENA ground-motion database and with the predictions from other relations.

The simulations to develop the ENA ground-motion prediction equations are based on the well-known stochastic method (Boore, 2003). The stochastic method has been used to derive ground-motion prediction equations for many different regions. Atkinson and Boore (1995) derived ground-motion prediction equations for ENA using a stochastic point-source model with an empirical two-corner source model. Toro *et al.* (1997) developed similar relations for ENA using a Brune single-corner frequency point-source model. Atkinson and Silva (2000) developed ground-motion prediction equations for California using a stochastic method that exploits the equivalence between the finite-fault model and a two-corner point-source model of the earthquake spectrum. In each of these cases, region-specific input parameters derived from seismograms were used to specify the model parameters that drive the ground-motion prediction equations for that region. For California, Atkinson and Silva (2000) showed that the stochastic prediction equations agree well with empirical regression equations for that region (e.g., Abrahamson and Silva, 1997; Boore *et al.*, 1997; Sadigh *et al.*, 1997). Stochastic ground-motion prediction equations provide a sound basis for estimating peak ground motions and response spectra for earthquakes of magnitudes 4 through 8, at distances from 1 to 200 km over the frequency range 0.2 to 20 Hz.

Stochastic Simulation Model

The stochastic model is a widely used tool to simulate acceleration time series and develop ground-motion prediction equations (Hanks and McGuire, 1981; Boore, 1983; Atkinson and Boore, 1995, 1997; Toro *et al.*, 1997; Atkinson and Silva, 2000; Boore, 2003). The stochastic method begins with the specification of the Fourier spectrum of ground motion as a function of magnitude and distance. The acceleration spectrum is typically modeled by a spectrum with an ω^2 shape, where ω = angular frequency (Aki, 1967; Brune, 1970, 1971; Boore 1983, 2003). The "ω^2 model" spectrum is derived for an instantaneous shear dislocation at a point. The acceleration spectrum of the shear wave, $A(f)$, at hypocentral distance R from an earthquake is given by:

$$A(f) = CM_0 (2\pi f)^2/[1 + (f/f_0)^2] \exp(-\pi f\kappa_0)\exp(-\pi fR/Q\beta)/R \quad (1)$$

where M_0 is seismic moment and f_0 is corner frequency, which is given by $f_0 = 4.9 * 10^6 \beta (\Delta\sigma/M_0)^{1/3}$ where $\Delta\sigma$ is stress parameter in bars, M_0 is in dyne centimeters, and β is shear-wave velocity in kilometers per second (Boore, 1983). The constant $C = \Re_{\theta\phi} FV/(4\pi\rho\beta^3)$, where $\Re_{\theta\phi}$ = radiation pattern (average value of 0.55 for shear waves), F = free-surface amplification (2.0), V = partition onto two horizontal components (0.71), ρ = density, and R = hypocentral distance (Boore, 1983). The term $\exp(-\pi f\kappa_0)$ is a high-cut filter to account for near-surface attenuation effects, which describe the commonly observed rapid spectral decay at high frequencies (Anderson and Hough, 1984). In equation (1) the power of R in the denominator of the attenuation term,

$\exp(-\pi fR/Q\beta)/R$, is equal to 1, which is appropriate for body-wave spreading in a whole space. This value can be changed as needed to account for deviations from $1/R$ due to factors such as postcritical reflections from the Moho discontinuity or multiply reflected waves traveling in the crustal waveguide. The quality factor, $Q(f)$, is an inverse measure of anelastic attenuation. Through this equation, the spectrum is diminished with distance to account for empirically defined attenuation behavior.

Finite-fault modeling has been an important tool for the prediction of ground motion near the epicenters of large earthquakes (Hartzell, 1978; Irikura, 1983; Joyner and Boore, 1986; Heaton and Hartzell, 1986; Somerville *et al.*, 1991; Tumarkin and Archuleta, 1994; Zeng *et al.*, 1994; Beresnev and Atkinson, 1998a,b). One of the most useful methods to simulate ground motion for a large earthquake is based on the simulation of many small earthquakes as subfaults that constitute an extended fault plane. A large fault is divided into N subfaults and each subfault is considered as a small point source (a method introduced by Hartzell, 1978). Ground motions of subfaults, each of which may be calculated by the stochastic point-source method as described previously, are summed with a proper time delay in the time domain to obtain the ground motion from the entire fault, $a(t)$:

$$a(t) = \sum_{i=1}^{nl} \sum_{j=1}^{nw} a_{ij}(t + \Delta t_{ij}), \qquad (2)$$

where nl and nw are the number of subfaults along the length and width of main fault, respectively ($nl * nw = N$), and Δt_{ij} is the relative time delay for the radiated wave from the ijth subfault to reach the observation point. The $a_{ij}(t)$ are each calculated by the stochastic point-source method (Boore, 1983, 2003).

In this study, we use a stochastic finite-fault approach, allowing us to incorporate significant finite-fault effects such as the geometry of larger ruptures and its effects on attenuation, and directivity. The simulations are performed with the computer code EXSIM (Extended Finite-Fault Simulation; Motazedian and Atkinson, 2005). This code is an updated version of the well-known FINSIM stochastic finite-fault model code (Beresnev and Atkinson, 1997a, 1998b, 2002). The modifications to FINSIM introduce the new concept of a "dynamic corner frequency," which decreases with time as the rupture progresses, to model more closely the effects of finite-fault geometry on the frequency content of radiated ground motions (Motazedian and Atkinson, 2005). The model has several significant advantages over previous stochastic finite-fault models, including independence of results from subfault size, conservation of radiated energy, and the ability to have only a portion of the fault active at any time during the rupture (simulating self-healing behavior [Heaton, 1990]).

EXSIM model parameters that represent the earthquake source processes have been calibrated for general applications, using data from 27 moderate to large well-recorded earthquakes in California (Motazedian and Atkinson, 2005). For use in ENA, the model requires region-specific source, attenuation, and generic site parameters, which are derived from recordings of small to moderate earthquakes.

We use EXSIM to simulate a ground-motion database from which to develop ground-motion equations. This approach is taken because there are not enough real data in the magnitude-distance ranges of engineering interest (**M** 5 to 7.5 at distances less than 200 km) to derive purely empirically based ground-motion prediction equations. We use the empirical data to establish the underlying parameters and validate the model predictions. The region-specific parameters needed for simulations are:

1. Attenuation of Fourier amplitudes with distance (apparent geometric spreading and Q-value)
2. Duration of ground motion as a function of magnitude and distance
3. Regional generic crust/site amplifications and physical constants
4. Source parameters for simulation: stress parameter and pulsing percentage. The stress parameter is most important because it controls the amplitudes of high-frequency radiation. The percentage of the fault that is pulsing at any time (simulating healing behavior as the rupture front passes) has an influence on the relative amount of low-frequency radiation. Simulated ground motions are sensitive to the stress parameter, but there is limited sensitivity to pulsing percentage. Thus stress is the key source parameter to be established. The stress parameter describes the level of the acceleration spectrum near the source, and is equivalent to the Brune model stress parameter as described by Boore (1983) and Atkinson and Boore (1995).

With these parameters established, we can use the calibrated EXSIM model to extend our predictions to the magnitude-distance range of interest. We then compare predictions with ENA data.

Model Parameters for Simulations and Their Uncertainty

The input model parameters for ENA ground-motion simulations are discussed next. For parameters with significant variability, we consider the effects of aleatory uncertainty, expressing random variability in the parameter from one ground-motion realization to another (Toro and McGuire, 1987). We do not attempt to model the effects of epistemic uncertainty (uncertainty in the correct median value of each parameter) in a comprehensive way in our simulations, because we do not believe this would be an appropriate way to deal with the broader issue of epistemic uncertainty in ground-motion prediction equations. To properly consider epistemic uncertainty, one needs to consider a wide variety of alternative models and theories of ground

motion, which is beyond our scope. Our scope is limited to defining our best estimate of ground motions for ENA and their aleatory uncertainty due to the natural random variability in earthquake source, path and site effects. However, we do consider the effect of epistemic uncertainty in the stress parameter on the results; limited knowledge concerning this parameter is the largest source of epistemic uncertainty in the prediction equations within the context of our model.

In the simulations to produce median ground-motion prediction equations, we include aleatory uncertainty by treating each key parameter as a probability distribution, with the given median value and the random variability about that median. Truncated normal or uniform distributions are used to express the uncertainty, depending on the parameter being modeled. The probability distributions model the random fluctuations in the actual effective values of the parameters that are observed from one ground-motion record to another, based on seismographic observations.

For example, the median value for stress in our simulations is 140 bars, based on the analysis of apparent source spectra from 36 ENA events of $\mathbf{M} \geq 4$. The log of the stress is a normally distributed parameter (mean log stress = 2.14) with standard deviation 0.31 log units (factor of 2 variability). Thus aleatory uncertainty in stress parameter is modeled using a normal distribution of log stress with mean 2.14 and standard deviation 0.31.

In the presentation of model parameters in the following sections, the median parameters are explained, along with the models used to represent aleatory uncertainty. Table 1 summarizes the median parameter values, whereas Table 2 presents the aleatory uncertainty. Uncertainty is included only for the key parameters that have a significant impact on predicted amplitudes. Other parameters, such as physical constants, are modeled with fixed parameter values.

Attenuation of Fourier Amplitudes with Distance. The attenuation of spectral amplitudes in ENA has recently been studied using a database of 1700 recordings of small to moderate ENA events recorded on hard-rock sites (Atkinson, 2004). This empirical study is a significant update of previous empirical models of attenuation (Atkinson and Mereu, 1992), including 10 more years of seismographic data, and incorporating newer three-component broadband data. The new analysis reveals that geometric spreading is significantly faster at near-source distances (<70 km) than was determined in previous studies. Specifically, Fourier amplitudes decay as $R^{-1.3}$ within 70 km of the source, then increase as $R^{+0.2}$ in the distance range from 70 km to 140 km (due to Moho bounce effects), then decrease as $R^{-0.5}$ at $R >$ 140 km. The associated Q-model is given by $Q = 893\,f^{0.32}$ with a minimum Q of 1000 (Atkinson, 2004). This attenuation model is used to diminish spectral amplitudes of subsource radiation with distance from the earthquake source.

Note that the attenuation model is not constrained by data within 10 km of the earthquake source. We assume that the near-source (<10 km) apparent geometric spreading for a point source is at the same rate as that observed from 10 to 70 km. In reality, the attenuation behavior inside 10 km is not known, and this is a source of uncertainty in the simulations at close distances.

Random variability in the rates of attenuation, and their effects on amplitudes at distance, is best modeled through the geometric-spreading coefficient, which is of most significance. In this study, based on detailed evaluation of the regression results of Atkinson (2004), the aleatory uncertainty in attenuation is modeled by normal distributions considering the geometric-spreading coefficient in the first 70 km to be given by -1.3 ± 0.1, and in the transition zone (70 to 140 km) by $+0.2 \pm 0.5$. This range of coefficients propagates attenuation uncertainty to larger distances

Table 1
Median Parameter Values for ENA Ground-Motion Simulations with EXSIM

Parameter	Median Value
Shear-wave velocity (at 13 km depth) (β)	3.7 km/sec
Density (at 13 km depth)	2.8 g/cm^3
Rupture propagation speed	0.8 β
Stress parameter	140 bars
Pulsing percentage	50%
Kappa	0.005
Geometric spreading, R^b: b =	-1.3 (0–70 km) $+0.2$ (70–140 km) -0.5 (>140 km)
Distance dependence of duration, d R, d =	0.0 (0–10 km) $+0.16$ (10–70 km) -0.03 (70–130 km) $+0.04$ (>130 km)
Quality factor	$Q = 893\,f^{0.32}$ ($Q_{\text{minimum}} = 1000$)
Fault dip	50°
Slip distribution and hypocenter location	Random

Table 2
Aleatory Uncertainty (Variability) in Key Model Parameters

Parameter	Distribution Type	Mean	Standard Deviation	Min	Max
Fault dip	truncated normal	50.	20.	10.	90.
Log stress	normal	2.14	0.31		
Pulsing percentage	uniform			10.	90.
Random site amplification (log units)	uniform	0.		-0.15	0.15
Kappa	uniform			0.002	0.008
b_1 ($R < 70$)	normal	-1.3	0.1		
b_2 (70–140)	normal	$+0.2$	0.5		
Depth	truncated normal	13.	10.	2.	30.
Fault length factor	truncated normal	0.6	0.2	0.2	1.0
Fault width factor	truncated normal	0.6	0.2	0.2	1.0

(>140 km) and is sufficient to model the net effects of uncertainty in all attenuation parameters. Note that attenuation uncertainties are coupled, such that uncertainties in geometric spreading and Q should not actually be treated as independent; mapping all of the attenuation uncertainty into geometric spreading is a simple way to approximate the expected overall behavior. We have not attempted to model the uncertainty in a detailed way, merely to mimic the behavior that is observed in ENA databases.

Atkinson (2004) found that the attenuation in ENA depends slightly on the focal depth of the earthquake, and proposed depth-correction factors to the attenuation model based on depth. These factors were not included in the simulations, because the attenuation rates are being randomized to account for their aleatory uncertainty, and the depth-correction factors to the attenuation are a relatively insignificant component of the overall attenuation; thus, depth effects on attenuation are considered part of the overall attenuation uncertainty modeled through the assumed variability in geometric-spreading rates.

Duration of Ground Motion. The duration (T) of an earthquake signal at hypocentral distance R can generally be represented as (Atkinson and Boore, 1995):

$$T(R) = T_0 + dR, \tag{3}$$

where T_0 is the source duration, and d is the coefficient controlling the increase of duration with distance; d is derived empirically. d may be a single coefficient describing all distances of interest (e.g., Atkinson, 1993b), or it can take different values depending on the distance range (e.g., Atkinson and Boore, 1995). The empirical duration model of Atkinson and Boore (1995) was adopted for this study. The duration increases in a hinged quadlinear fashion from the source, mimicking the form of the attenuation model. The coefficients for d are 0.0, 0.16, -0.03, and 0.04, for the distance ranges 0 to 10 km, 10 to 70 km, 70 to 130 km, and >130 km, respectively (see Atkinson and Boore, 1995). In Atkinson and Boore (1995), the zero distance duration was 0.0 sec; here we let it be 1.0 sec. The source duration is estimated as the subfault rise time, as determined by the subfault radius and the rupture-propagation speed. We re-examined this duration model in light of recent data, and saw no evidence that this model should be revised. The uncertainty in duration is not modeled, as it is less significant than uncertainty in other parameters in terms of its impact on simulated ground-motion amplitudes.

Regional Generic Crust/Site Amplifications and Physical Constants. The shear-wave velocity (β) at average focal depths (near 13 km) is assumed to be 3.7 km/sec, with density (ρ) 2.8 g/cm^3. These are typical regional values (Boore and Joyner, 1997). Shear-wave velocity actually depends on depth, so in the modeling of alternative focal depths (discussed in a following section), the value of β is selected based on the event depth, such that β increases from a value of 3.1 km/sec at a depth of 5 km, through the value of 3.7 km/sec at 13 km, to a maximum of 3.8 km/sec for depths of 14.5 km or more. These values were based on typical crustal shear-wave velocity profiles (e.g., Somerville *et al.*, 2001). The physical constants are not a significant source of uncertainty.

Amplification of horizontal-component ground motions, for rock sites, occurs because of the combined effects of the velocity gradient in the crust and near-surface amplification due to the weathered layer of rock in the top few meters. (There is additional site response for soil sites, but this is not considered within the simulations; modifications to model soil sites by applying additional soil amplifications are discussed later.) An approximation of the amount of amplification for rock sites may be obtained empirically using the horizontal-to-vertical component ratios (H/V ratios) for rock sites in ENA, as discussed by Atkinson (2004). The basic idea is that amplification of the vertical component is very small compared with that of the horizontal component, allowing H/V to provide a first-order site-amplification estimate. A criticism of the H/V technique, as originally applied to microtremor measurements (e.g., Nakamura's technique), is that it is largely a measure of Rayleigh wave ellipticity. However, it has been pointed out that when applied to body waves, as measured from earthquakes, the H/V ratio may be largely controlled by site response (Lermo and Chavez-Garcia, 1993). Several studies support the hypothesis of Lermo and Chavez-Garcia (1993) that the observed H/V ratios are a measure of the amplification of seismic ground motions due to their transit through the crustal and/or near-surface velocity gradient. For example, Atkinson and Cassidy (2000) show that the H/V ratio for rock sites in western British Columbia matches the amplification that would be expected based on the regional shear-wave velocity gradient. The expected amplification was calculated from the regional shear-wave velocity profile, using the quarter-wavelength approximation (Boore and Joyner, 1997) to estimate the amplification as a function of frequency. Atkinson and Cassidy (2000) also studied ground motions for soft soil sites in the Fraser Delta, British Columbia, that amplify weak

Table 3
Site Amplification Factors Used in the Simulations for Hard-Rock Sites, NEHRP A

Frequency (Hz)	Amplification Factor
0.5	1.
1.	1.13
2.	1.22
5.	1.36
10.	1.41
50.	1.41

Assumed shear-wave velocity near the surface of ≥2000 m/sec, no profile defined. Amplification is empirical (based on Siddiqqi and Atkinson, 2002).

motions three to five times in the frequency range from 0.3 to 4 Hz, and concluded that observed amplifications were consistent with the H/V ratios. Siddiqqi and Atkinson (2002) report a similar finding for rock sites in different environments across Canada, including eastern Canada.

The assumed amplification for ENA rock sites increases from a value of 1.0 for frequencies less than 0.5 Hz, to a value of 1.41 at $f \geq 10$ Hz, as given by Siddiqqi and Atkinson (2002). Table 3 provides the amplification factors used for the hard-rock site simulations (NEHRP A); Table 4 provides those that apply for NEHRP B/C boundary site conditions (discussed later in the text). The high-frequency amplification factor for hard rock ($=1.4$) is consistent with near-surface shear-wave velocities of about 2 km/sec, according to simple calculations with the quarter-wavelength impedance-based method of Boore and Joyner (1997) (e.g., $\sqrt{3.7/1.9} = 1.4$). These inferred near-surface velocities for hard-rock sites in ENA are consistent with estimates based on shear-wave refraction studies (Beresnev and Atkinson, 1997b).

Variability in site amplification is modeled by using an additional amplification factor randomly drawn from a uniform distribution ranging from -0.15 to $+0.15$ log units for each trial. In the aleatory sense, this uncertainty represents the typical random variability that is seen even among nearby sites with apparently similar site conditions (Boore, 2004).

Amplification effects are counteracted at high frequencies by the effects of the high-frequency shape factor κ_0 (Anderson and Hough, 1984). κ_0 acts to diminish spectral amplitudes rapidly at high frequencies, and is believed to be primarily a site effect. For hard-rock sites in ENA, the effects of κ_0 are nearly negligible. Atkinson (1996) estimated a κ_0 value of 0.002. In this study, a careful examination of the spectral data presented by Atkinson (2004) was made to search for the values of κ_0 to use in the simulations. This indicated a minimum κ_0 of 0, with a maximum value for individual records of 0.01. The aleatory uncertainty in κ_0 is represented by a uniform distribution from 0.002 to 0.008. As discussed later, the simulation results are not sensitive to the kappa parameter, except for response spectra at frequencies > 20 Hz.

Table 4
Site Amplification Factors Used in the Simulations for NEHRP B/C Boundary ($V_{30} = 760$ m/sec)

Frequency (Hz)	Amplification Factor
0.0001	1.000
0.1014	1.073
0.2402	1.145
0.4468	1.237
0.7865	1.394
1.3840	1.672
1.9260	1.884
2.8530	2.079
4.0260	2.202
6.3410	2.313
12.540	2.411
21.230	2.452
33.390	2.474
82.000	2.497

Amplification is based on square-root-impedance calculations and the velocity model in Table A6 of Frankel *et al.* (1996).

Source Parameters for Simulation. The most important source parameter for the simulations is the stress parameter, which controls the spectral amplitudes at high frequencies. The distribution of this parameter was determined from the high-frequency level of apparent source spectra for all ENA events of $\mathbf{M} \geq 4$, as listed in Table 5, at a reference distance of 20 km (denoted A_{hf} (20 km)). The source spectra for instrumentally recorded earthquakes were determined by using the attenuation model of Atkinson (2004) to correct all vertical-component observations on rock back to the reference distance of 20 km; the vertical component data on rock are used as they are relatively free from site-amplification effects. Note that this attenuation correction assumes a point source, which will be adequate for most of the instrumental events because of their small to moderate size. The source spectrum of an event was obtained by averaging the log amplitudes at this reference distance over all stations that recorded the event. The stress was then defined as the Brune stress value associated with this high-frequency spectral level; this value was determined using equation (1), with the parameter values adopted in this study. This stress value also assumes a point source (Brune model). The frequency range used to determine the high-frequency level was 5 to 10 Hz for the events with modern instrumental data. For early-instrumental data from large ENA events (Atkinson and Chen, 1997), the maximum available frequencies are in the range from 1.5 to 2 Hz; for these events this frequency range was used to define A_{hf}, under the assumption that earthquakes of $\mathbf{M} > 6$ will have corner frequencies less than 1 Hz. High-frequency spectral levels were also estimated for pre-instrumental events based on their felt area. As shown by Atkinson (1993a), the felt area of an earthquake is well correlated with high-frequency spectral level. The empirical relationship of Atkinson (1993a) between these two parameters was updated in this study to include all events through 2003 with both determined spectral levels and felt areas. The new relationship for A_{hf} (20 km) based on felt area is shown in Figure 1 and given by:

$$\log A_{hf}\ (20\ \text{km}) = -4.78 + 0.92 \log A_{\text{felt}} \qquad (4)$$

where A_{hf} (20 km) is in centimeters per second and A_{felt} is in kilometers squared. This relationship was used in Table 5 to determine the point-source stress parameter for events having no modern instrumental data, but a well-determined felt area. In preparing Table 5, only events with a known moment magnitude (from independent studies) were considered, except for the 1811 New Madrid and 1886 Charleston events, which were assigned nominal moment magnitudes

of 7.5 and 7.0, respectively (see Johnston, 1996; Hough *et al.*, 2000).

On Figure 2, the high-frequency spectral levels for ENA events (from Table 5) are plotted versus **M**, along with the predicted behavior for both Brune point-source and EXSIM finite-fault models. The Brune model predictions are precise, as they are analytically specified (equation 1), whereas the EXSIM values are not. The EXSIM values were obtained by performing trial simulations with different input values of stress, for fault distances of approximately 20 km, and obtaining average Fourier accelerations in this distance range. They are intended to show overall trends only. Note that the EXSIM predictions appear very similar to the Brune point-source predictions for a given stress at magnitudes less than 6. At larger magnitudes, the EXSIM model predicts lower near-source motions than the point source due to finite-fault effects; this is because much of the extended fault plan is far away from the observation point. This trend is believed to be responsible for the conclusion of some studies that, when using a point-source model, a decreasing trend in stress with increasing magnitude is obtained (e.g., as discussed in Atkinson and Silva, 2000).

Overall, we conclude from Figure 2 that there is no evidence of a decreasing trend of stress with increasing magnitude. Furthermore, the determination of a stress parameter near 200 bars for the 2001 **M** 7.7 Bhuj, India earthquake (Singh *et al.*, 2004) argues against a decreasing stress trend for large intracontinental events. If anything, Figure 2 sug-

Table 5

Stress Parameters for ENA Events of $\mathbf{M} \geq 4$ Based on High-Frequency Spectral Level at 20 km (A_{hf})

Year	Month	Day	Moment **M**	log A_{hf} (20 km)	Reference	$\Delta\sigma$ (bars)	Instrumental	$\Delta\sigma$ EXSIM (bars)
1811			7.5	1.66	MMI	175	0	
1886			7	1.38	MMI	160	0	
1925	3	1	6.4	1.27	MMI	310	0	
1929	8	12	4.9	0.43	MMI	230	0	
1929	11	18	7.3	1.55	MMI	170	0	
1935	11	1	6.2	1.19	MMI	325	0	
1939	10	19	5.3	0.63	MMI	230	0	
1940	12	20	5.5	0.66	MMI	180	0	
1944	9	5	5.8	0.77	MMI	155	0	
1968	11	9	5.4	1.05	MMI	800	0	
1980	8	27	5.1	0.67	MMI	380	0	
1982	1	9	4.6	−0.01	MMI	90	1	
1982	1	9	5.5	0.58	MMI	135	1	
1982	1	11	5.2	0.37	A2004	110	1	
1982	1	19	4.3	−0.13	A2004	110	1	
1982	3	31	4.2	−0.15	A2004	120	1	
1982	6	16	4.2	−0.23	A2004	90	1	
1983	10	7	5.0	0.51	A2004	260	1	
1985	10	5	6.7	1.22	A1993	155	1	
1985	12	23	6.8	1.12	A1993	90	1	134
1985	12	25	5.2	0.22	A1993	65	1	
1986	1	31	4.8	0.32	A2004	190	1	
1986	7	12	4.5	0.15	A2004	185	1	
1987	6	10	5.0	0.55	A1993	290	1	
1988	3	25	6.3	0.92	A1993	110	1	
1988	11	23	4.3	−0.18	A2004	90	1	
1988	11	25	5.8	1.28	BA92	500	1	500
1989	3	16	5.0	0.47	A1993	230	1	
1989	12	25	5.9	0.97	A1993	260	1	
1990	10	19	4.7	0.33	A2004	250	1	250
1997	11	6	4.5	−0.14	A2004	70	1	104
1998	9	25	4.5	0.40	A2004	440	1	
1999	3	16	4.5	0.04	A2004	130	1	85
2000	1	1	4.7	0.22	A2004	160	1	105
2002	4	20	5.0	0.07	A2004	55	1	149
2005	3	6	5.0	0.30	AB2005	120	1	125

Reference MMI indicates A_{hf} inferred from intensity data, A1993 indicates A_{hf} from spectral data of Atkinson (1993a), A2004 indicates A_{hf} from spectral data of Atkinson (2004). Value for 6 March 2005 event was determined in this study. A_{hf} is in cgs units. Instrumental = 1 indicates instrumental determination with modern digital data. $\Delta\sigma$ EXSIM is best input subfault stress to EXSIM to match response spectra data for well-recorded events.

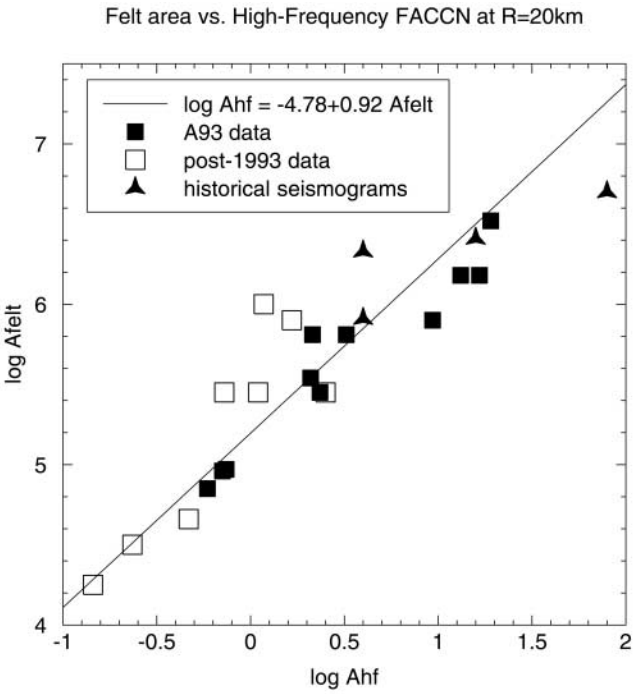

Figure 1. Relationship between felt area and high-frequency spectral acceleration level (at a reference distance of 20 km). Filled squares, data from Atkinson (1993a); open squares, new data from Atkinson (2004); filled triangles, historical seismogram data of Atkinson and Chen (1997). Lines show least-squares fit.

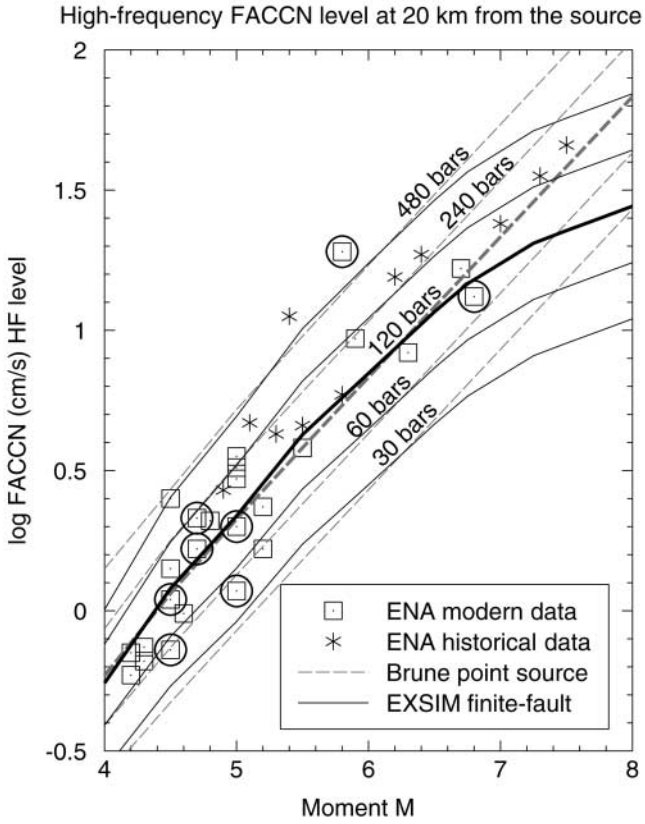

Figure 2. ENA high-frequency spectral level at 20 km compared with predictions of Brune point-source and EXSIM finite-fault models (approximate). Circled events are well-recorded events discussed in the text.

gests an increase of stress with magnitude, in particular, in the context of the finite-fault model. However, the data are weak for $\mathbf{M} \geq 6$, and are subject to particularly large uncertainties because most of the high-magnitude data are based on inferences from poor-quality historical seismograms or intensity data. Furthermore, the large-earthquake data were interpreted in the context of a point-source model in deriving the values of A_{hf} (20 km).

To gain further insight into the value of stress that should be used in the EXSIM modeling, the best EXSIM subfault stress was determined for the well-recorded ENA events in the database (Ⓔ available in the electronic edition of BSSA). There are eight such events. This determination was carried out using the generic model parameters of this study, rather than trying to define event-specific geometries and parameters and perform detailed modeling studies (which would be beyond our scope). In this exercise, all input parameters adopted in this study for the ground-motion model are assumed, and the stress parameter is varied to find the value that minimizes the average data residuals at 5 to 10 Hz for all stations within 800 km. The stress values obtained in this manner are listed for the eight well-recorded events on Table 5. The previously reported value of 500 bars for the Saguenay event is retained in this table because of the mismatch of residuals at large distances (which imply stress $<$400 bars) with those at stations in the Charlevoix region near 100 km (which imply stress $>$1000 bars). The (log) average value of EXSIM stress for these eight events is 150 bars, or 130 bars if the problematic Saguenay event is excluded. (The average of the point-source stress values for the same eight events is 135 bars, including Saguenay). The eight modeled events are circled on Figure 2.

It is apparent from inspection of Table 5 that the EXSIM stress values inferred by modeling the pseudo-acceleration spectra (PSA) values do not closely match the values inferred from the Fourier data for the same events, projected back to 20 km (although the average values are similar). Thus the computed stress parameter is sensitive to how it is derived. Differences between evaluating Fourier spectra in the context of a point-source attenuation model, and evaluating response spectra in the context of a finite-fault model, can be significant. Furthermore, Figure 2 is based on interpretation of vertical-component data, whereas the PSA modeling uses horizontal-component data where available.

Based on the inferred EXSIM stress for the best-recorded events, we adopt a median stress parameter of 140 bars. In the EXSIM simulations, uncertainty in stress is represented by a normal distribution in log stress with mean 2.14 log units and standard deviation of 0.31 units (e.g., a factor of 2 variability in stress parameter represents 1 standard devi-

ation). Other interpretations of the data in Table 5 are possible, leading to other alternative values for the stress parameter. We provide a mechanism for adjusting the equations to model a higher- or lower-stress parameter; these adjustments may be useful in the interpretation of specific events, or in modeling epistemic uncertainty in predictions due to uncertainty in the median stress parameter.

Another issue that arises in assigning the stress-parameter distribution is an apparent difference in the median stress for the instrumental data and that inferred from the historical data, as can be seen on Figure 2. This could be interpreted in the context of an increasing trend of stress parameter with magnitude, because of the relative distribution of the data sources in magnitude (historical data dominate the large-magnitude data). Due to the large uncertainties in the historical data as mentioned previously, we do not consider the apparent differences in stress compelling. Furthermore, finite-fault modeling of data in regions such as California, which have better data coverage at higher magnitudes, favor constant-stress or decreasing-stress scaling with increasing magnitude (Atkinson and Silva, 1997, 2000). Therefore, we retain a constant-stress-scaling model for the predictions. Description of the source properties remains our biggest source of uncertainty in modeling ENA ground motions, and the area that most needs improvement in the future.

The percentage-pulsing area describes how much of the fault plane in slipping at any moment in time. This parameter is assumed based on calibration studies with California data (Motazedian and Atkinson, 2005). It is assigned a relatively large aleatory variability, represented by a uniform distribution from 10% to 90%. This parameter is not well determined, but does not exert a significant influence on the simulated amplitudes at most frequencies (it exerts some influence at lower frequencies, as discussed by Motazedian and Atkinson, 2005).

Earthquake focal depths in ENA cover a broad range from a few kilometers to 30 km. Recent depth determinations (Ma and Atkinson, 2006) were used to determine a mean focal depth of 13 km. Depth is assumed to be truncated-normally distributed, with a standard deviation of 10 km. The normal distribution is truncated to provide a minimum depth of 2 km, and maximum depth of 30 km. This depth is used to fix the center of the fault plane for the simulations, in the vertical dimension. Once the location of the fault plane within the crust is fixed, the subfault at which the rupture is assumed to initiate is drawn randomly.

The geometry of the fault plane and its placement within the crust is treated as follows. The fault dip is assumed to be a normally distributed random variable with a value of 50 ± 20 degrees. The fault length and width, which are functions of magnitude, are also considered uncertain. EXSIM assumes the fault lengths and widths given by the global empirical relationships of Wells and Coppersmith (1994). However, recent data suggest that ENA fault dimensions are probably significantly smaller for a given moment magnitude (Somerville *et al.*, 2001). This effect is modeled by multiplying the fault length and width obtained by the Wells and Coppersmith relations by a normally distributed factor, taken as 0.6 ± 0.2 for both length and width; the distributions are truncated to stipulate a minimum factor of 0.2 and maximum factor of 1.0. The net effect of these factors is to assign a fault area that is on average about one third the equivalent fault area for events in active tectonic regions. These factors do not have a significant impact on predicted amplitudes, except for very large events ($\mathbf{M} > 7$). Just for the geometric purposes of placing the fault within the crust, it is assumed that the depth of the hypocenter corresponds to the middle of the fault width; if this implies a surface rupture, the fault width extends from the surface to the depth indicated by the fault width and dip. When generating the ground motions, the actual location of the hypocenter on the fault plane is assumed to be random, as is the slip distribution. (Thus the actual depth of the hypocenter will not match the focal depth used to define the midpoint of the fault for an individual simulation, but will match in an average sense over many simulations.)

Results

Simulations were performed using the EXSIM model with the median parameters as listed in Table 1, including aleatory uncertainty as given by the distributions in Table 2. Ground motions from 10 earthquakes with moment magnitudes from 3.5 to 8.0 were simulated, in 0.5 magnitude unit increments, at 24 values of fault distances ranging from 1 to 1000 km. (Note, the actual fault distances simulated are as follows: 1, 2, 5, 10, 15, 20, 30, 40, 50, 60, 70, 80, 100, 120, 150, 200, 250, 300, 400, 500, 600, 700, 800, and 1000 km.) Eight lines at equally spaced azimuths spreading out from a point above the center of the top of the fault plane were defined to capture the average effects of directivity; the geometry of the simulated points is shown in Figure 3. The details of capturing the directivity effects (e.g., azimuthally

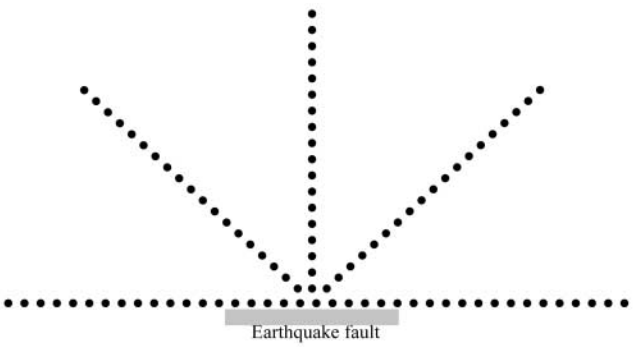

Figure 3. Geometry of sites for simulations. Locations of sites step out from a point above the center of the fault plane, along eight lines equally spaced in azimuth. Only one half of the focal sphere is shown in the figure (lines are symmetrical about fault).

determined lines or a "racetrack" of points at fixed distance) are relatively unimportant because of the numerous distances and magnitudes simulated, which effectively act to randomize the geometry. Tests were performed to confirm that the results are unchanged if the number of simulated azimuths is doubled or quadrupled. For each magnitude and observation point, 20 random trials were performed. Thus a total of 38,400 horizontal-component ground-motion records were simulated (10*24*8*20), all for hard-rock sites. These records were used to compute 5% damped PSA as well as PGA and PGV.

Figure 4 plots response spectral amplitudes from the simulations (including aleatory variability) versus closest distance to the fault for magnitudes 5 and 8. It may be ob-

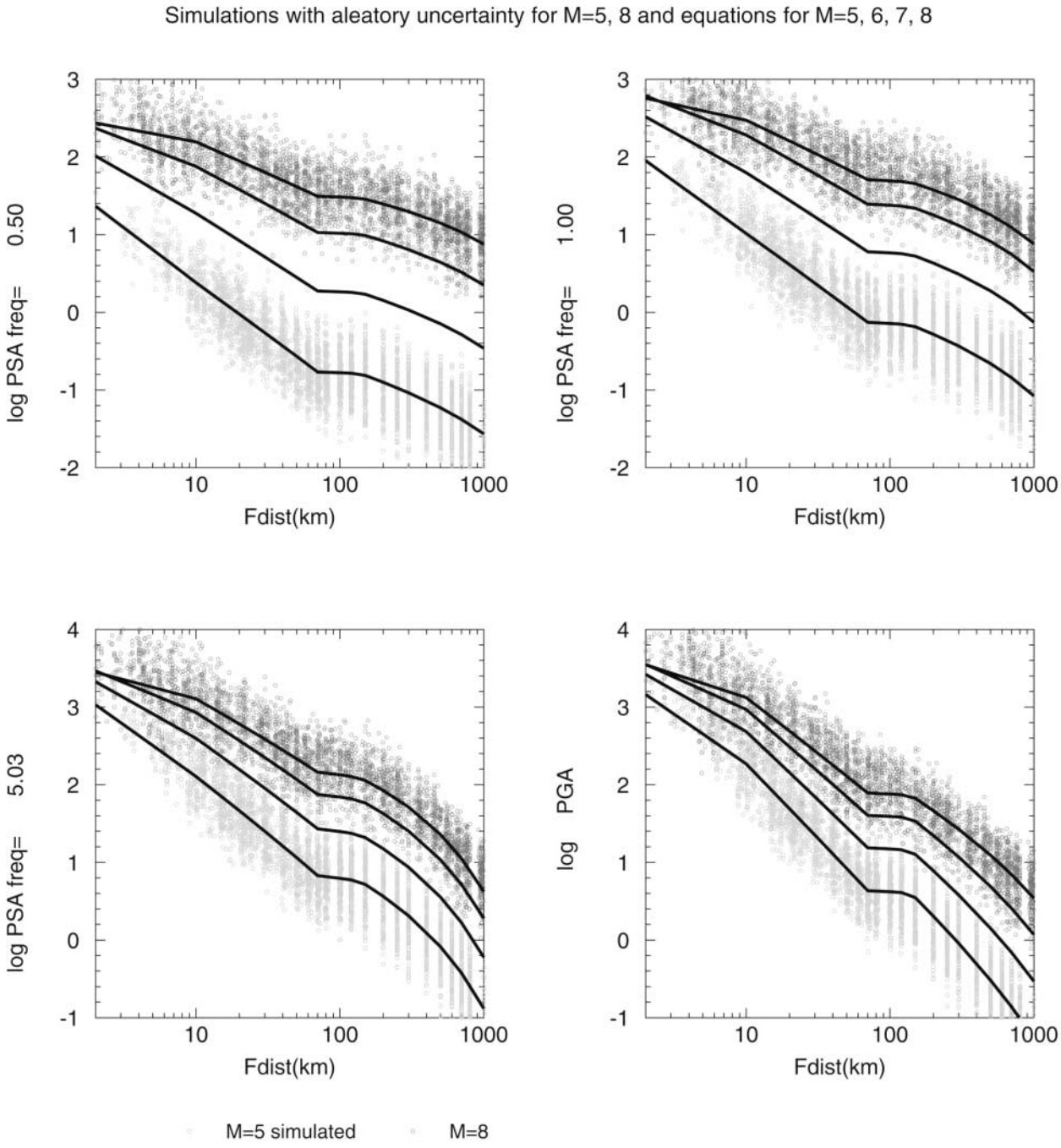

Figure 4. Log values of horizontal component 5% pseudo-acceleration at frequencies 0.5, 1, and 5 Hz, and PGA, for ENA rock sites. Dots show PSA from simulations, including aleatory uncertainty, for **M** 5 (light) and **M** 8 (dark). Solid lines show predicted amplitudes from regression equations developed from simulated database, for **M** 5, 6, 7, and 8.

served that the highest simulated amplitudes have been truncated in the *y* scale chosen for the plots. The highest spectral amplitudes, as well as the highest simulated PGA, reach 4.6 log units for a few of the most extreme points (**M** 8 at 1 km). We make no claims that such amplitudes are physically possible—they are merely the result of the simulation exercise, which does not account for factors that may act to limit extreme amplitudes. The figure also plots curves that represent the median amplitudes for **M** 5, 6, 7, and 8. The median values for near-source amplitudes from large events (3.5 log units at high frequencies and PGA) appear reasonable for a very hard rock-site condition. The curves were determined by a standard regression analysis to an equation in moment magnitude (**M**) and closest distance to the fault (R_{cd}) of the form:

$$\begin{aligned}\text{Log PSA} = {} & c_1 + c_2\mathbf{M} + c_3\mathbf{M}^2 + (c_4 + c_5\mathbf{M})f_1 \\ & + (c_6 + c_7\mathbf{M})f_2 + (c_8 + c_9\mathbf{M})f_0 \\ & + c_{10}R_{cd} + S,\end{aligned} \tag{5}$$

where $f_0 = \max(\log(R_0/R_{cd}), 0)$; $f_1 = \min(\log R_{cd}, \log R_1)$; $f_2 = \max(\log(R_{cd}/R_2), 0)$; $R_0 = 10$; $R_1 = 70$; $R_2 = 140$; and $S = 0$ for hard-rock sites; its value for soil sites is discussed in the next section and given in equation (7a),(7b). Note that this form assumes linearity of motions for hard-rock sites, but can accommodate nonlinearity for soil sites (equation 7a,7b).

The coefficients of the equation are given in Table 6. The equations do an excellent job of reproducing the simulations; there are no significant residual trends with distance or magnitude, as shown for an example magnitude (**M** 6) on Figure 5. The aleatory uncertainty is independent of magnitude and distance, with an average value of 0.30 log units for all frequencies. This calculated variability, based purely on the simulation parameters, is slightly larger than typically observed values for empirical strong ground motion prediction equations in California (e.g., Boore *et al.*, 1997; Abrahamson and Silva, 1997). The amount of variability in the simulations is consistent with that observed in the ENA data, and may reflect the apparently large variability in ENA stress parameters. On the other hand, one could argue that the variability of ground motions should be the same in ENA as it is in California, in which case the simulated variability may slightly overestimate the actual variability. Note, though, that recent estimates of variability of ground motions for active tectonic regions (Boore and Atkinson, 2006) also tend to be slightly larger than previous estimates for California (e.g., Boore *et al.*, 1993). The variability issue will require further ENA data before it is resolved.

On Figure 6, we compare these new prediction equations with the previous relations of Atkinson and Boore (1995) (table version). The range of new ENA ground-motion prediction equations proposed by EPRI (2004) is also shown; the EPRI prediction equations are represented by a set of 12 alternative equations with weights, which we have simplified for plotting by showing the mean and standard deviation of the predictions from the 12 relations. Our new prediction equations are similar to the AB95 prediction equations. The main difference is that high-frequency amplitudes ($f \geq 5$ Hz) are less than previously predicted (by about a factor of 1.6 within 100 km), because of a slightly lower average stress parameter (140 bars versus 180 bars) and a steeper near-source attenuation. Our model now includes a small amount of amplification for hard-rock sites, which offsets to some extent the differences due to the factors listed previously. The model also features a higher kappa in comparison with our previous model ($\kappa_0 = 0.005$ versus f_{max} [high-cut filter] = 50 Hz). However, we performed parametric sensitivity studies that showed that, with the exception of predicted ground motions for $f > 20$Hz, the results are not sensitive to the choice of a kappa distribution from 0.002 to 0.008, versus the use of a fixed $f_{max} = 50$ Hz. The reason is that a damped oscillator responds to frequencies at or below its natural frequency. The influence of energy at lower frequencies results in the response spectra predictions, and the PGA prediction, being insensitive to kappa over our frequency range of interest. Thus the choice of kappa is not important and not a factor in the differences between our current predictions and those of AB95.

The new model can be used to predict ground motions much closer to the fault (this is applicable for large events that may rupture to the surface), due to the improved consideration of finite-fault effects; however, remember that the values at close distances (<10 km) are model based rather than empirically driven. The treatment of finite-fault effects is also important in providing an improved scaling of motions with magnitude, in particular, at closer distances. We note that the magnitude/distance saturation effects predicted by the simulations are in qualitative accord with effects seen in empirical databases from active tectonic regions (Boore and Atkinson, 2006). In detail, though, the empirical saturation effects are stronger than those predicted by our simulations, in particular, for large magnitudes (**M** $\geq$ 7) at distances within 50 km. The new model also explicitly provides site-amplification factors for a full range of shear-wave velocities, as described in the next section, leading to less ambiguity in interpretation of the results for soil sites. The overall similarity of the new prediction equations to those of Atkinson and Boore (1995) is interesting, given the increase in database and new simulation methodology used in this study. It lends weight to previous conclusions that a two-corner point-source model can be used to mimic salient finite-fault effects in the development of ground-motion prediction equations (Atkinson and Silva, 2000).

It is critical to compare the predicted ground motions with observations to assess their overall reliability. We compiled response spectra data for rock sites in ENA, based on data presented by Atkinson and Boore (1998), Atkinson and Chen (1997), and Atkinson (2004). In addition, the Bhuj, India, observations of Cramer and Kumar (2003) are included, corrected to hard-rock site conditions by using the

Table 6

Coefficients of Equations for Predicting Median ENA Ground Motions on Hard Rock (Horizontal Component, log(10) Values Are Given in cgs Units) for 5% Damped PSA at Stated Frequencies, According to Equation (5)

Frequency (Hz)	Period (sec)	c_1	c_2	c_3	c_4	c_5	c_6	c_7	c_8	c_9	c_{10}
0.20	5.00	−5.41E+00	1.71E+00	−9.01E−2	−2.54E+00	2.27E−01	−1.27E+00	1.16E−01	9.79E−01	−1.77E−01	−1.76E−04
0.25	4.00	−5.79E+00	1.92E+00	−1.07E−01	−2.44E+00	2.11E−01	−1.16E+00	1.02E−01	1.01E+00	−1.82E−01	−2.01E−04
0.32	3.13	−6.04E+00	2.08E+00	−1.22E−01	−2.37E+00	2.00E−01	−1.07E+00	8.95E−02	1.00E+00	−1.80E−01	−2.31E−04
0.40	2.50	−6.17E+00	2.21E+00	−1.35E−01	−2.30E+00	1.90E−01	−9.86E−01	7.86E−02	9.68E−01	−1.77E−01	−2.82E−04
0.50	2.00	−6.18E+00	2.30E+00	−1.44E−01	−2.22E+00	1.77E−01	−9.37E−01	7.07E−02	9.52E−01	−1.77E−01	−3.22E−04
0.63	1.59	−6.04E+00	2.34E+00	−1.50E−01	−2.16E+00	1.66E−01	−8.70E−01	6.05E−02	9.21E−01	−1.73E−01	−3.75E−04
0.80	1.25	−5.72E+00	2.32E+00	−1.51E−01	−2.10E+00	1.57E−01	−8.20E−01	5.19E−02	8.56E−01	−1.66E−01	−4.33E−04
1.0	1.00	−5.27E+00	2.26E+00	−1.48E−01	−2.07E+00	1.50E−01	−8.13E−01	4.67E−02	8.26E−01	−1.62E−01	−4.86E−04
1.3	0.794	−4.60E+00	2.13E+00	−1.41E−01	−2.06E+00	1.47E−01	−7.97E−01	4.35E−02	7.75E−01	−1.56E−01	−5.79E−04
1.6	0.629	−3.92E+00	1.99E+00	−1.31E−01	−2.05E+00	1.42E−01	−7.82E−01	4.30E−02	7.88E−01	−1.59E−01	−6.95E−04
2.0	0.500	−3.22E+00	1.83E+00	−1.20E−01	−2.02E+00	1.34E−01	−8.13E−01	4.44E−02	8.84E−01	−1.75E−01	−7.70E−04
2.5	0.397	−2.44E+00	1.65E+00	−1.08E−01	−2.05E+00	1.36E−01	−8.43E−01	4.48E−02	7.39E−01	−1.56E−01	−8.51E−04
3.2	0.315	−1.72E+00	1.48E+00	−9.74E−02	−2.08E+00	1.38E−01	−8.89E−01	4.87E−02	6.10E−01	−1.39E−01	−9.54E−04
4.0	0.251	−1.12E+00	1.34E+00	−8.72E−02	−2.08E+00	1.35E−01	−9.71E−01	5.63E−02	6.14E−01	−1.43E−01	−1.06E−03
5.0	0.199	−6.15E−01	1.23E+00	−7.89E−02	−2.09E+00	1.31E−01	−1.12E+00	6.79E−02	6.06E−01	−1.46E−01	−1.13E−03
6.3	0.158	−1.46E−01	1.12E+00	−7.14E−02	−2.12E+00	1.30E−01	−1.30E+00	8.31E−02	5.62E−01	−1.44E−01	−1.18E−03
8.0	0.125	2.14E−01	1.05E+00	−6.66E−02	−2.15E+00	1.30E−01	−1.61E+00	1.05E−01	4.27E−01	−1.30E−01	−1.15E−03
10.0	0.100	4.80E−01	1.02E+00	−6.40E−02	−2.20E+00	1.27E−01	−2.01E+00	1.33E−01	3.37E−01	−1.27E−01	−1.05E−03
12.6	0.079	6.91E−01	9.97E−01	−6.28E−02	−2.26E+00	1.25E−01	−2.49E+00	1.64E−01	2.14E−01	−1.21E−01	−8.47E−04
15.9	0.063	9.11E−01	9.80E−01	−6.21E−02	−2.36E+00	1.26E−01	−2.97E+00	1.91E−01	1.07E−01	−1.17E−01	−5.79E−04
20.0	0.050	1.11E+00	9.72E−01	−6.20E−02	−2.47E+00	1.28E−01	−3.39E+00	2.14E−01	−1.39E−01	−9.84E−02	−3.17E−04
25.2	0.040	1.26E+00	9.68E−01	−6.23E−02	−2.58E+00	1.32E−01	−3.64E+00	2.28E−01	−3.51E−01	−8.13E−02	−1.23E−04
31.8	0.031	1.44E+00	9.59E−01	−6.28E−02	−2.71E+00	1.40E−01	−3.73E+00	2.34E−01	−5.43E−01	−6.45E−02	−3.23E−05
40.0	0.025	1.52E+00	9.60E−01	−6.35E−02	−2.81E+00	1.46E−01	−3.65E+00	2.36E−01	−6.54E−01	−5.50E−02	−4.85E−05
PGA	0.010	9.07E−01	9.83E−01	−6.60E−02	−2.70E+00	1.59E−01	−2.80E+00	2.12E−01	−3.01E−01	−6.53E−02	−4.48E−04
PGV	0.011	−1.44E+00	9.91E−01	−5.85E−02	−2.70E+00	2.16E−01	−2.44E+00	2.66E−01	8.48E−02	−6.93E−02	−3.73E−04

Total sigma = 0.30 for all frequencies.

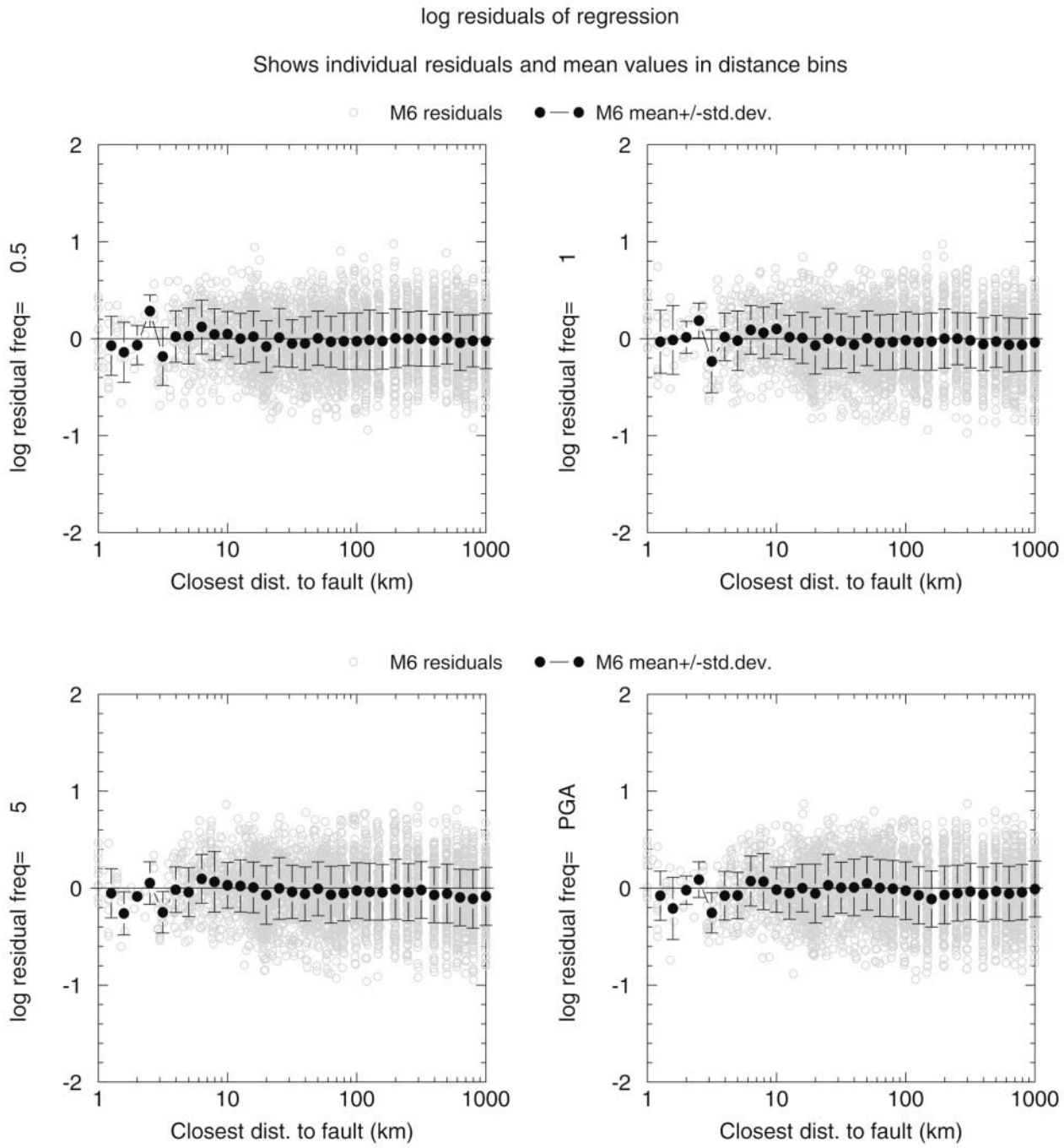

Figure 5. Example of regression residuals versus distance for **M** 6. Gray dots are individual residuals (where log residual = log simulated PSA — log PSA predicted by equation 5). Filled symbols show mean residuals and standard deviation in distance bins.

site-condition factors adopted for this study (as described in the next section). The Bhuj data (26 January 2000) are included because of the suggested similarity of the Bhuj and New Madrid earthquakes (Cramer and Kumar, 2003; Bodin and Horton, 2004; Singh *et al.*, 2004), but their relevance is less certain than that of the other data, in particular, in light of the need to make site corrections to obtain equivalent values for hard-rock conditions. Ⓔ The ENA response spectra data are provided in the electronic edition of BSSA.

The ENA data (horizontal component or equivalent) have been plotted on Figure 7 in comparison with the ground-motion prediction equations (simulations and equations), at two representative frequencies (1 and 5 Hz). The prediction equations appear to be in reasonable agreement with the data, with some exceptions. Most notably, the equations underpredict a cluster of enhanced high-frequency amplitude data for **M** 5.5 ($\pm$0.5) near 100 km. This cluster represents strong-motion observations from the **M** 5.8 1988

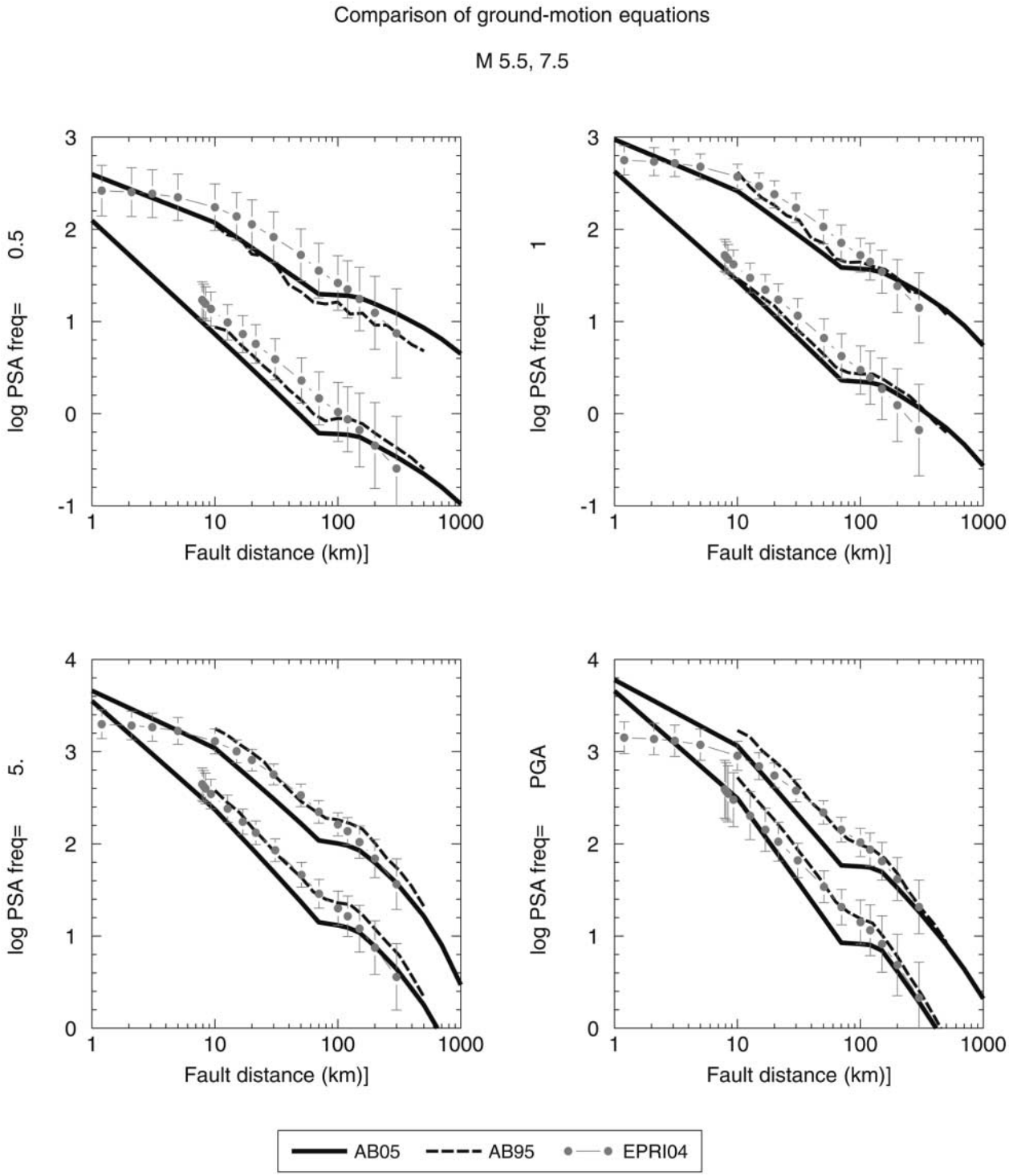

Figure 6. Comparison of ground-motion equations of this study (solid black lines) for **M** 5.5 and 7.5, with previous predictions (Atkinson and Boore, 1995), and mean and standard deviation of alternative EPRI (2004) predictions, all for hard-rock site conditions in ENA.

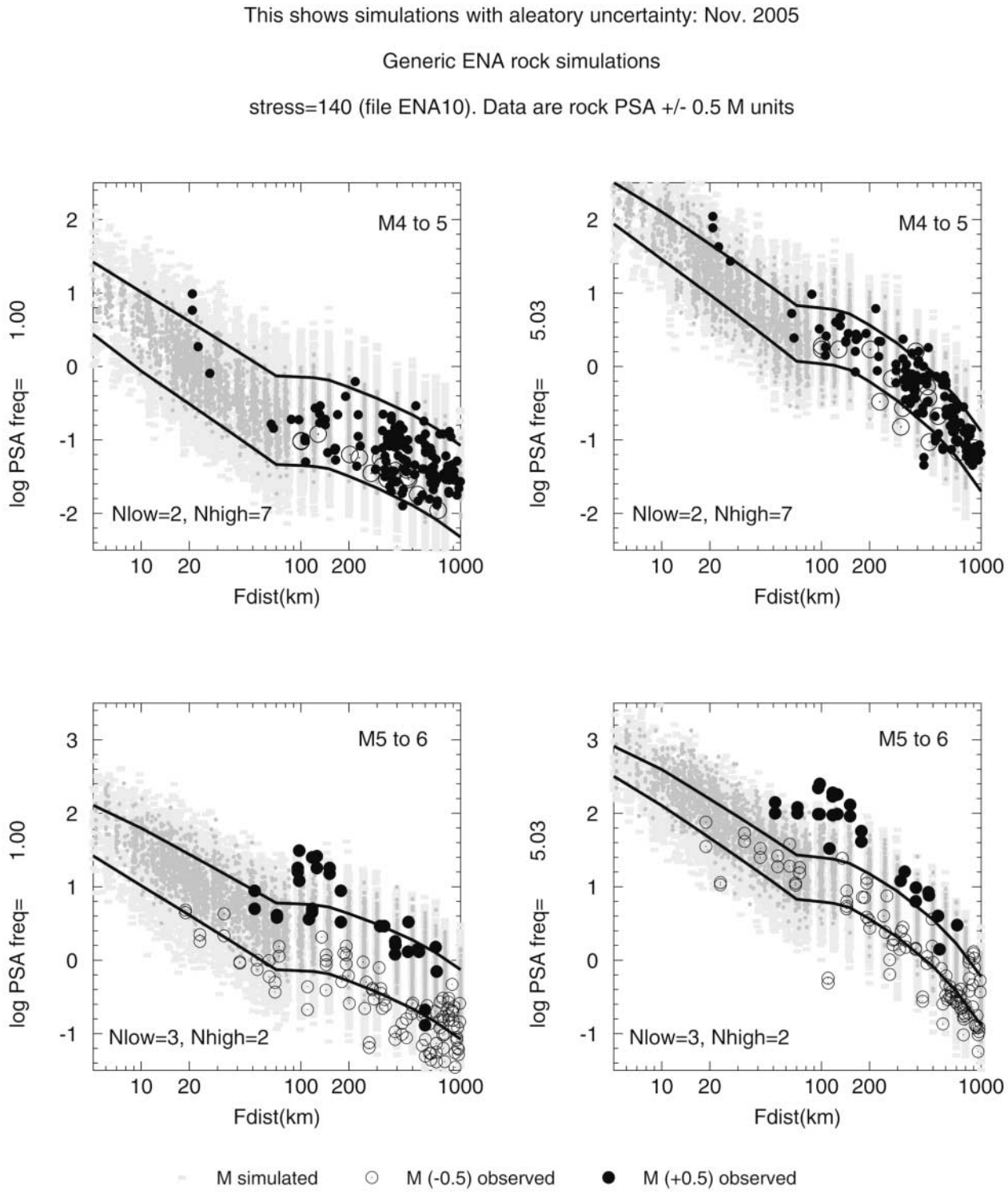

Figure 7. Comparison of ENA rock simulations (gray dots) and prediction equations (lines) with ENA rock data within stated magnitude ranges. Data include both horizontal components where available; where only the vertical component was recorded, this is converted to equivalent horizontal using the amplification factors of Table 3. Open symbols show data in lower half of magnitude range; filled symbols show data in upper half of range; the number of events within each range is given at the lower left corner of each panel. Heavier gray denotes simulations at central magnitude of range, light gray is ± 0.5 units. Lines show prediction equation values for lower and upper bounds of stated magnitude ranges. (*continued*)

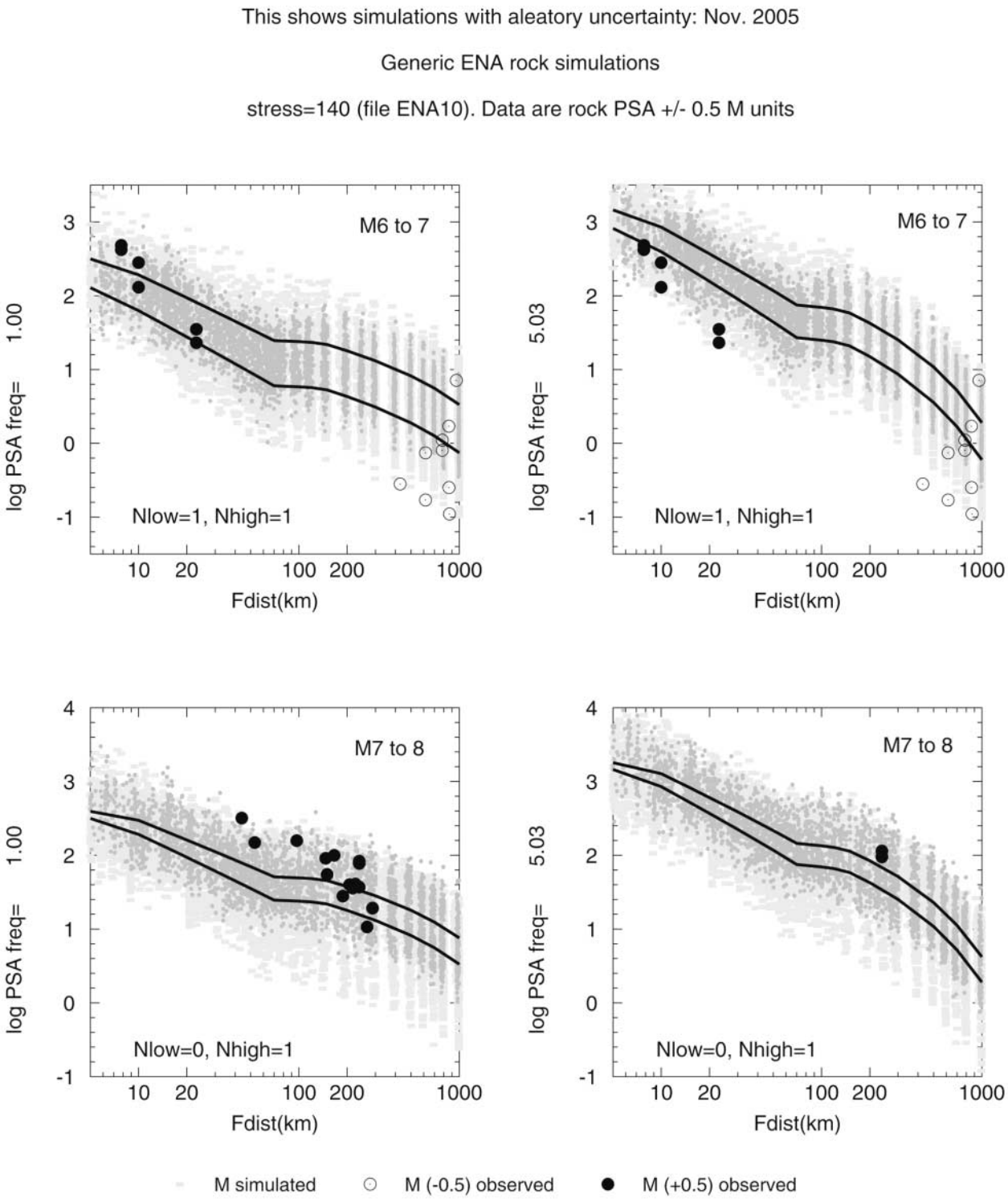

Figure 7. Continued.

Saguenay, Quebec, earthquake (25 November 1988), which had particularly strong high-frequency amplitudes (Boore and Atkinson, 1992). The high-frequency amplitudes from the Saguenay event are nearly as large as those for the Bhuj earthquake, despite the large difference in their magnitudes. This point is emphasized by comparing Saguenay versus Bhuj amplitudes on Figure 8, for intermediate frequencies (1 Hz) and high frequencies (PGA).

Ideally, the simulations would show close agreement with the data over all magnitudes and distances. However, the key model parameters (such as the stress parameter and attenuation) were estimated from a different empirical database than that represented by the available ground-motion data for validation (although considerable overlap exists). In particular, the attenuation model is based on a much larger ENA database that includes many smaller events not used in the comparisons shown here. Thus there is no guarantee of a close match between the ground-motion database and the simulated amplitudes at all magnitudes and distances, given the interplay between various parameters. Indeed, it was not an aim of the simulations to match the subset of ENA data that is available for the magnitude-distance range of engineering interest, as this subset is too limited to be definitive with regard to the important parameters (especially attenuation).

It is illuminating to examine in more detail the data from the moderate events that appear to have significant average residuals at distances less than 100 km. Figure 9 plots the ground-motion amplitudes from the well-recorded **M** 5.0 2006 Riviere du Loup earthquake in comparison with the prediction equations of this study. The equations predict the data well at lower frequencies, but at higher frequencies there are positive residuals in the distance range from 30 to 70 km. For this event, it appears that the data would prefer a higher stress parameter with steeper near-source attenuation (although this would overpredict the closest data points). On Figure 10, amplitudes are plotted for three events of **M** 4.5 in relation to the prediction equations. The shape of the attenuation appears approximately correct for these events.

Examining the residuals (ratio of observed amplitude to predicted amplitude) indicates that the prediction equations agree well with available ENA ground-motion data overall: there are near-zero average residuals (within a factor of 1.2) for all frequencies, and there are no statistically significant residual trends with distance. However, there is a tendency to positive residuals for moderate events at high frequencies in the distance range from 30 to 100 km (by as much as a factor of 2), due largely to contributions from the Saguenay and Riviere du Loup events. This indicates epistemic uncer-

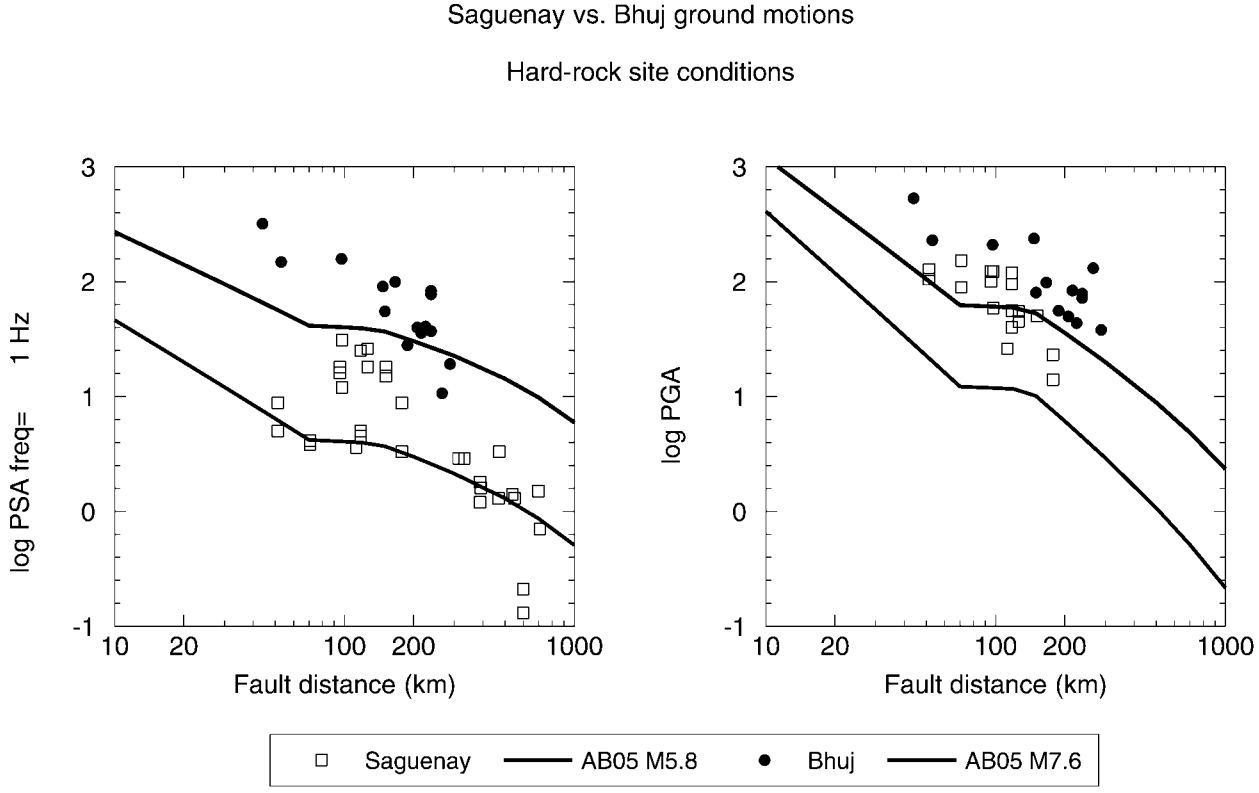

Figure 8. Comparison of ground-motion amplitudes from **M** 5.8 Saguenay, Quebec, earthquake and **M** 7.6 Bhuj, India, earthquake, for hard-rock conditions. Prediction equations of this study are also shown.

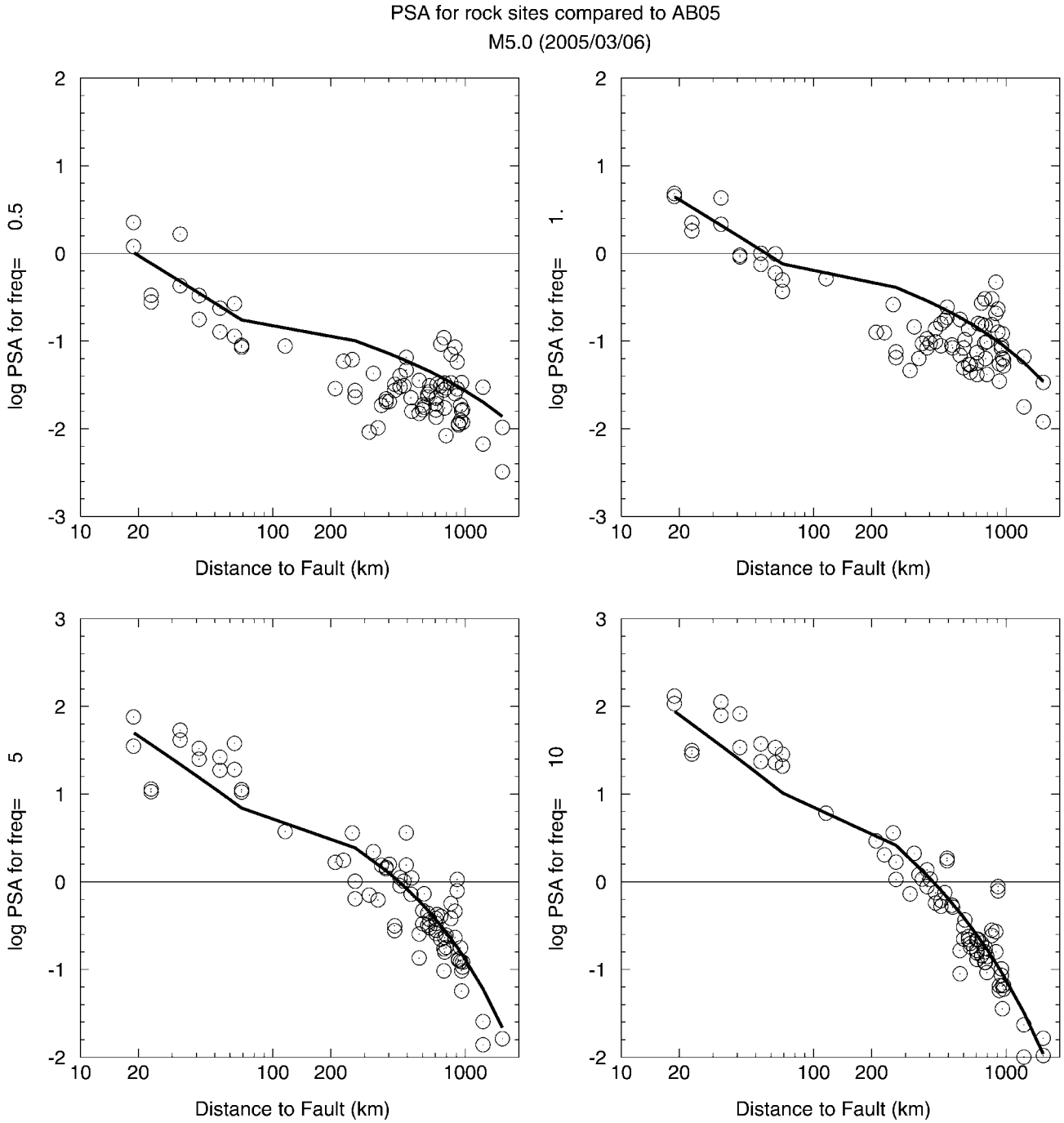

Figure 9. Comparison of ground-motion amplitudes for **M** 5.0 2005 Riviere du Loup earthquake with predictive equations (horizontal component), for rock sites, at frequencies of 0.5, 1, 5, and 10 Hz.

tainty in the prediction model. The positive residuals for moderate events at <100 km could be eliminated by an increased stress parameter, at the cost of producing negative residuals in other magnitude-distance ranges. In acknowledgment of this uncertainty, it is useful to define adjustment factors to the equations that may be used to model the effects of a different stress parameter on the equations.

Adustment of Equations to Consider Alternative Stress Parameters

Uncertainty in the stress parameter is the largest source of epistemic uncertainty in the ENA ground-motion equations. The equations were developed for a stress of 140 bars, but the limitations in our knowledge are such that the epistemic uncertainty in this value is likely of the order of a

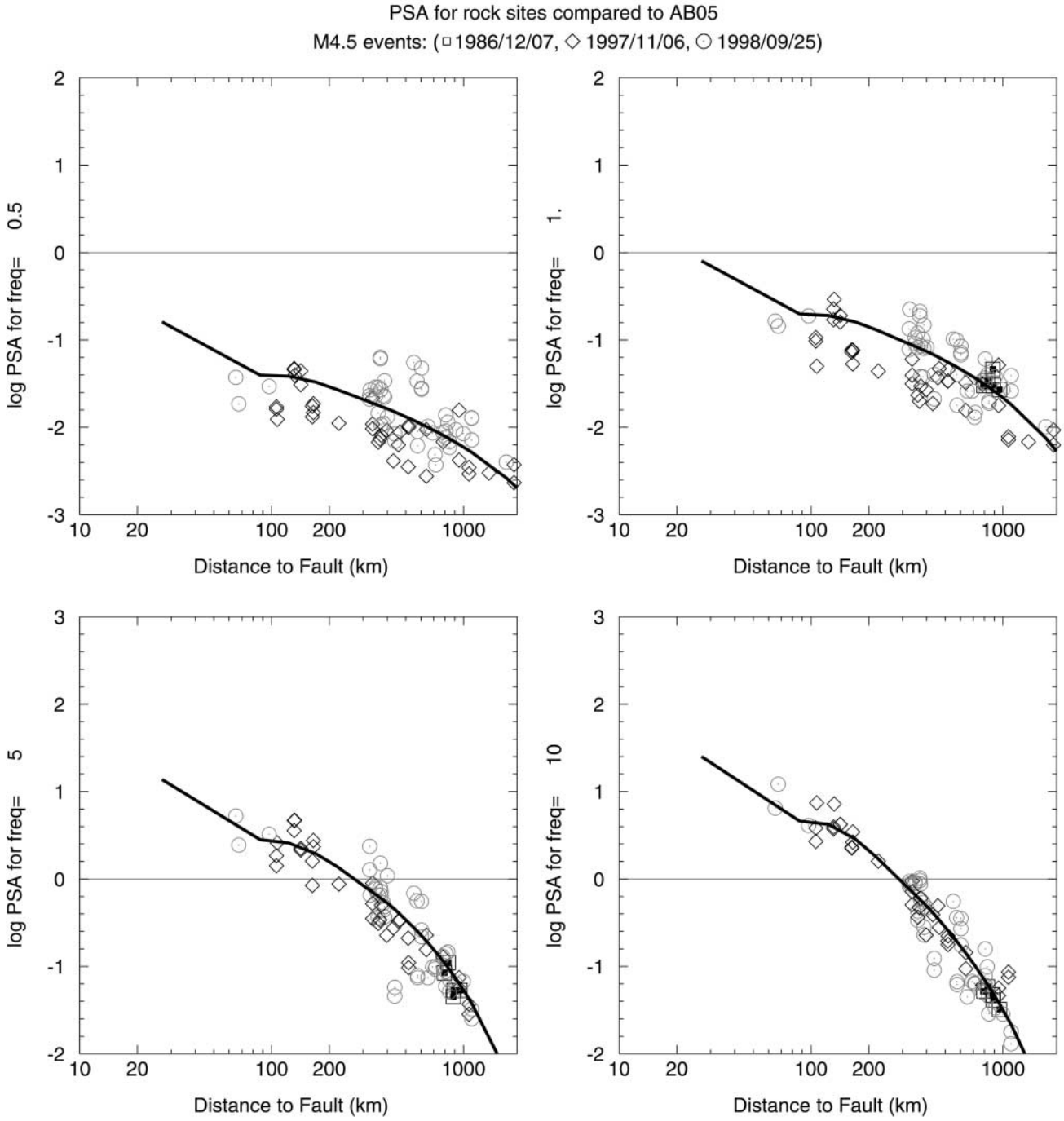

Figure 10. Comparison of ground-motion amplitudes for four events of **M** 4.5 with predictive equations (horizontal component or equivalent), for rock sites, at frequencies of 0.5, 1, 5, and 10 Hz.

factor of 1.5 to 2. By repeating the EXSIM simulations for the parameters of Table 1, but varying the stress parameter, the effect of the stress parameter on the simulated PSA values was defined. The effect is approximately independent of distance. It varies with magnitude and frequency because of the corner-frequency effect of the source spectrum. Specifically, increasing the stress parameter has a near-zero effect at low frequencies, then results in increasing PSA until a constant factor is reached at high frequencies; the frequency range over which the increase in amplitude will occur depends on magnitude. The effect is illustrated in Figure 11, which plots the amount by which the log PSA amplitudes predicted by equation (5) would need to be increased to accommodate a factor of 2 increase in stress parameter (i.e., a stress parameter of 280 bars). The stress-adjustment factor for a factor of 2 in stress can be modeled (within about 5%) by the fol-

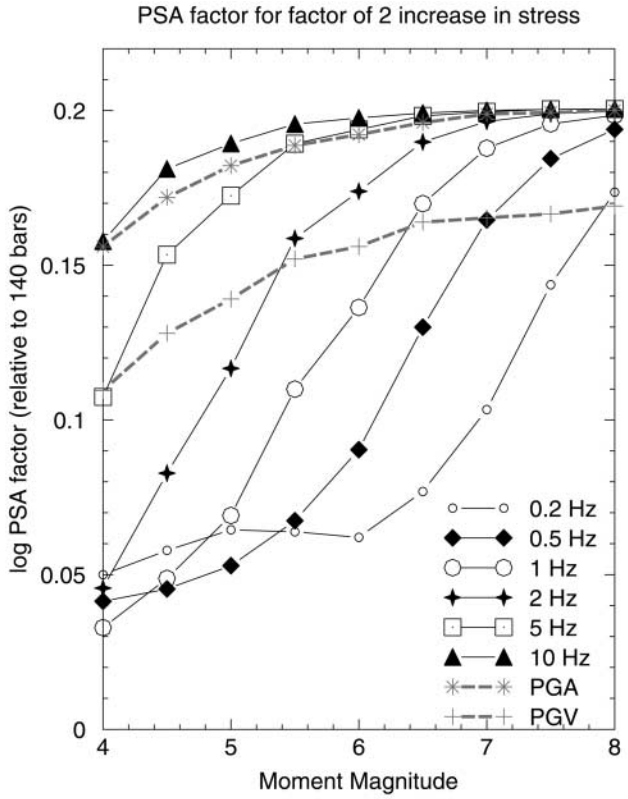

Figure 11. Effect on predicted ground-motion amplitudes of increasing the stress parameter by a factor of 2 (relative to predicted values for 140 bars).

lowing equation, for which the coefficients are provided in Table 7:

$$\text{Log } SF_2 = \min\{[\Delta + 0.05], [0.05 + \Delta \{\max[(\mathbf{M} - M_1), 0.] / (M_h - M_1)]\}] \quad (6)$$

Thus to predict the amplitudes for an event with stress = 280 bars, we would compute log PSA (equation 5) + log SF_2. For other stress values greater than 140 bars, a scaled factor can be used; for example, for a factor of 1.5 on stress (=210 bars), we would compute log PSA (equation 5) + (1.5/2) log SF_2. For stress values smaller than 140 bars, we subtract the equivalent factors; for example, for a stress of 140/1.5 = 93 bars, we would compute log PSA (equation 5) − (1.5/2) log SF_2. These factors can be used to provide alternative equations that model epistemic uncertainty in median stress, or to interpret the best stress parameter for specific recorded events. The scaled equation is adequate for consideration of stress parameters within a factor of 4 of 140 bars (e.g., 35 to 560 bars), but has not been tested beyond this range.

Equations for Soil Sites

The equations presented previously and given in Table 6 are for hard-rock sites ($\beta \geq 2000$ m/sec, or NEHRP site class A). For other NEHRP site classes, the amplification factors can be derived on the basis of empirical studies of ground-motion data from datarich regions. Boore *et al.* (1997) presented such amplification factors as a function of shear-wave velocity in the upper 30 m (V_{30}), based on ground-motion data recorded at various site conditions in California, and assuming linear soil response. Recent studies (Choi and Stewart, 2005) based on large worldwide strong-motion databases have validated the Boore *et al.* factors for the linear range of response, but shown that a nonlinear correction needs to be applied for sites that experience strong shaking (defined as expected rock PGA > 60 cm/sec^2). Boore and Atkinson (2006) presented factors to account for soil amplification in both the linear and nonlinear ranges as follows:

$$S = \log\{\exp[b_{\text{lin}} \ln(V_{30}/V_{\text{ref}}) + b_{nl} \ln (60/100)]\} \quad \text{for pgaBC} \leq 60 \text{ cm/sec}^2 \quad (7a)$$

and

$$S = \log\{\exp[b_{\text{lin}} \ln(V_{30}/V_{\text{ref}}) + b_{nl} \ln (\text{pgaBC}/100)]\}, \quad \text{for pgaBC} > 60 \text{ cm/sec}^2 \quad (7b)$$

where pgaBC is the predicted value of PGA for V_{30} = 760m/sec. The form of the linear factor (7a) is taken from Boore *et al.* (1997), but with Choi and Stewart's (2005) coefficients (similar to those of Boore *et al.* [1997], but extending to lower frequency). The nonlinear factor is controlled by the slope b_{nl}, as given by the following function, which was derived by simplifying the empirical results derived by Choi and Stewart (2005):

$$b_{nl} = b_1 \qquad \text{for } V_{30} \leq v_1 \quad (8a)$$

$$b_{nl} = (b_1 - b_2) \ln(V_{30}/v_2)/\ln(v_1/v_2) + b_2 \qquad \text{for } v_1 < V_{30} \leq v_2 \quad (8b)$$

$$b_{nl} = b_2 \ln(V_{30}/V_{\text{ref}})/\ln(v_2/V_{\text{ref}}) \qquad \text{for } v_2 < V_{30} \leq V_{\text{ref}} \quad (8c)$$

$$b_{nl} = 0.0 \qquad \text{for } V_{30} > V_{\text{ref}} \quad (8d)$$

In these equations, the amplification is given relative to the reference condition of NEHRP B/C boundary, with V_{ref} = 760 m/sec (see Table 8 for other coefficient values). The equations are robust for conditions softer than V_{ref}, but are not empirically constrained for sites with high shear-wave velocities. The reference-site condition (V_{ref}) is significantly softer than the hard-rock condition that applies to the predictions developed in this study and presented in Table 6. To allow application of the empirically based soil factors to ENA, we therefore develop a separate set of ENA ground-motion prediction equations for the NEHRP B/C boundary-

Table 7
Coefficients of Stress Adjustment Factors (Equation 6)

Frequency (Hz)	Δ	M_l	M_h
0.20	0.15	6.00	8.50
0.25	0.15	5.75	8.37
0.32	0.15	5.50	8.25
0.40	0.15	5.25	8.12
0.50	0.15	5.00	8.00
0.63	0.15	4.84	7.70
0.80	0.15	4.67	7.45
1.00	0.15	4.50	7.20
1.26	0.15	4.34	6.95
1.59	0.15	4.17	6.70
2.00	0.15	4.00	6.50
2.52	0.15	3.65	6.37
3.17	0.15	3.30	6.25
3.99	0.15	2.90	6.12
5.02	0.15	2.50	6.00
6.32	0.15	1.85	5.84
7.96	0.15	1.15	5.67
10.02	0.15	0.50	5.50
12.62	0.15	0.34	5.34
15.89	0.15	0.17	5.17
20.00	0.15	0.00	5.00
25.18	0.15	0.00	5.00
31.70	0.15	0.00	5.00
39.91	0.15	0.00	5.00
PGA	0.15	0.50	5.50
PGV	0.11	2.00	5.50

Table 8
Coefficients for Soil Response, as Given in Equations (7) and (8)

Frequency (Hz)	b_{lin}	b_1	b_2
0.2	−0.752	−0.300	0
0.25	−0.745	−0.310	0
0.32	−0.740	−0.330	0
0.5	−0.730	−0.375	0
0.63	−0.726	−0.395	0
1	−0.700	−0.440	0
1.3	−0.690	−0.465	−0.002
1.6	−0.670	−0.480	−0.031
2	−0.600	−0.495	−0.060
2.5	−0.500	−0.508	−0.095
3.2	−0.445	−0.513	−0.130
4	−0.390	−0.518	−0.160
5	−0.306	−0.521	−0.185
6.3	−0.280	−0.528	−0.185
8	−0.260	−0.560	−0.140
10	−0.250	−0.595	−0.132
12.6	−0.232	−0.637	−0.117
15.9	−0.249	−0.642	−0.105
20	−0.286	−0.643	−0.105
25	−0.314	−0.609	−0.105
32	−0.322	−0.618	−0.108
40	−0.330	−0.624	−0.115
PGA	−0.361	−0.641	−0.144
PGV	−0.600	−0.495	−0.060

At all frequencies, $V_{ref} = 760$, $v_1 = 180$, $v_2 = 300$.

site condition. This involves redoing the simulations, but replacing the crustal amplification model that is applicable to hard rock ($V_{30} \geq 2000$ m/sec) with one that is applicable to a near-surface velocity of 760 m/sec in ENA; we used the model given in Table A6 of Frankel *et al.* (1996), but with a source velocity of 3.7 km/sec rather than 3.6 km/sec. The amplification model was derived using the square-root-impedance method of Boore and Joyner (1997; see also Boore, 2003), in which amplification is computed based on the seismic-impedance gradient; for each frequency, the depth corresponding to a quarter wavelength is calculated, and the amplification is estimated based on the square root of the seismic-impedance ratio between the source region and the quarter-wavelength depth. Table 4 presents the resulting amplification factors.

The amplification factors of Table 4 are multiplied by the $\exp(-\pi f\kappa_0)$ operator in the simulations. For hard-rock sites, κ_0 was assumed to be uniformly distributed between 0.002 and 0.008 (see Table 1). For NEHRP B/C boundary-site conditions, we assume κ_0 is uniformly distributed between 0.01 and 0.03.

The simulations for NEHRP B/C boundary conditions were regressed to equation (5) to determine the coefficients for the prediction equations as given in Table 9. The prediction equations of Table 9 can be used with the soil response factors of Boore and Atkinson (2006), as given in equation (7a),(7b) with the coefficients as listed in Table 8, to calculate expected ENA ground motions for any specified V_{30}. This makes the implicit assumption that relative amplification effects of different soil conditions in ENA are the same as those for active tectonic regions. Note that the stress-amplification factors of equation (6) can be applied to the B/C boundary predictions to consider alternative values of the stress parameter.

Figure 12 compares the equations of this study for NEHRP B/C boundary-site conditions with the empirical relations of Boore and Atkinson (2006), for active tectonic regions, for the same shear-wave velocity. The amplitudes from the relations are broadly similar at low frequencies, albeit with very different functional shapes for the relations. At high frequencies, the differences are more pronounced; this study suggests that ENA amplitudes scale more strongly with magnitude at high frequencies than is suggested by empirical strong-motion data from active regions. ENA high-frequency amplitudes are larger than those in active regions, especially at large distances (>200 km) and close to the source (<20 km). The empirical relations suggest stronger near-source distance saturation than is provided by the simulations of this study; the implication is that the equations for ENA may overpredict near-source motions, if there are significant saturation effects that are not accounted for in the simulation model. These effects will require further evaluation by comparing ENA data more closely with data from active tectonic regions.

Table 9

Coefficients of Equations for Predicting Median ENA Ground Motions for BC Boundary (V_{30} = 760 m/sec) (Horizontal Component, log(10) Values Are Given in cgs Units) for 5% Damped PSA at Stated Frequencies, According to Equation (5)

Frequency (Hz)	Period (sec)	c_1	c_2	c_3	c_4	c_5	c_6	c_7	c_8	c_9	c_{10}
0.20	5.00	−4.85E+00	1.58E+00	−8.07E−02	−2.53E+00	2.22E−01	−1.43E+00	1.36E−01	6.34E−01	−1.41E−01	−1.61E−04
0.25	4.00	−5.26E+00	1.79E+00	−9.79E−02	−2.44E+00	2.07E−01	−1.31E+00	1.21E−01	7.34E−01	−1.56E−01	−1.96E−04
0.32	3.13	−5.59E+00	1.97E+00	−1.14E−01	−2.33E+00	1.91E−01	−1.20E+00	1.10E−01	8.45E−01	−1.72E−01	−2.45E−04
0.40	2.50	−5.80E+00	2.13E+00	−1.28E−01	−2.26E+00	1.79E−01	−1.12E+00	9.54E−02	8.91E−01	−1.80E−01	−2.60E−04
0.50	2.00	−5.85E+00	2.23E+00	−1.39E−01	−2.20E+00	1.69E−01	−1.04E+00	8.00E−02	8.67E−01	−1.79E−01	−2.86E−04
0.63	1.59	−5.75E+00	2.29E+00	−1.45E−01	−2.13E+00	1.58E−01	−9.57E−01	6.76E−02	8.67E−01	−1.79E−01	−3.43E−04
0.80	1.25	−5.49E+00	2.29E+00	−1.48E−01	−2.08E+00	1.50E−01	−9.00E−01	5.79E−02	8.21E−01	−1.72E−01	−4.07E−04
1.0	1.00	−5.06E+00	2.23E+00	−1.45E−01	−2.03E+00	1.41E−01	−8.74E−01	5.41E−02	7.92E−01	−1.70E−01	−4.89E−04
1.3	0.794	−4.45E+00	2.12E+00	−1.39E−01	−2.01E+00	1.36E−01	−8.58E−01	4.98E−02	7.08E−01	−1.59E−01	−5.75E−04
1.6	0.629	−3.75E+00	1.97E+00	−1.29E−01	−2.00E+00	1.31E−01	−8.42E−01	4.82E−02	6.77E−01	−1.56E−01	−6.76E−04
2.0	0.500	−3.01E+00	1.80E+00	−1.18E−01	−1.98E+00	1.27E−01	−8.47E−01	4.70E−02	6.67E−01	−1.55E−01	−7.68E−04
2.5	0.397	−2.28E+00	1.63E+00	−1.05E−01	−1.97E+00	1.23E−01	−8.88E−01	5.03E−02	6.84E−01	−1.58E−01	−8.59E−04
3.2	0.315	−1.56E+00	1.46E+00	−9.31E−02	−1.98E+00	1.21E−01	−9.47E−01	5.58E−02	6.50E−01	−1.56E−01	−9.55E−04
4.0	0.251	−8.76E−01	1.29E+00	−8.19E−02	−2.01E+00	1.23E−01	−1.03E+00	6.34E−02	5.81E−01	−1.49E−01	−1.05E−03
5.0	0.199	−3.06E−01	1.16E+00	−7.21E−02	−2.04E+00	1.22E−01	−1.15E+00	7.38E−02	5.08E−01	−1.43E−01	−1.14E−03
6.3	0.158	1.19E−01	1.06E+00	−6.47E−02	−2.05E+00	1.19E−01	−1.36E+00	9.16E−02	5.16E−01	−1.50E−01	−1.18E−03
8.0	0.125	5.36E−01	9.65E−01	−5.84E−02	−2.11E+00	1.21E−01	−1.67E+00	1.16E−01	3.43E−01	−1.32E−01	−1.13E−03
10.0	0.100	7.82E−01	9.24E−01	−5.56E−02	−2.17E+00	1.19E−01	−2.10E+00	1.48E−01	2.85E−01	−1.32E−01	−9.90E−04
12.6	0.079	9.67E−01	9.03E−01	−5.48E−02	−2.25E+00	1.22E−01	−2.53E+00	1.78E−01	1.00E−01	−1.15E−01	−7.72E−04
15.9	0.063	1.11E+00	8.88E−01	−5.39E−02	−2.33E+00	1.23E−01	−2.88E+00	2.01E−01	−3.19E−02	−1.07E−01	−5.48E−04
20.0	0.050	1.21E+00	8.83E−01	−5.44E−02	−2.44E+00	1.30E−01	−3.04E+00	2.13E−01	−2.10E−01	−9.00E−02	−4.15E−04
25.2	0.040	1.26E+00	8.79E−01	−5.52E−02	−2.54E+00	1.39E−01	−2.99E+00	2.16E−01	−3.91E−01	−6.75E−02	−3.88E−04
31.8	0.031	1.19E+00	8.88E−01	−5.64E−02	−2.58E+00	1.45E−01	−2.84E+00	2.12E−01	−4.37E−01	−5.87E−02	−4.33E−04
40.0	0.025	1.05E+00	9.03E−01	−5.77E−02	−2.57E+00	1.48E−01	−2.65E+00	2.07E−01	−4.08E−01	−5.77E−02	−5.12E−04
PGA	0.010	5.23E−01	9.69E−01	−6.20E−02	−2.44E+00	1.47E−01	−2.34E+00	1.91E−01	−8.70E−02	−8.29E−02	−6.30E−04
PGV	0.011	−1.66E+00	1.05E+00	−6.04E−02	−2.50E+00	1.84E−01	−2.30E+00	2.50E−01	1.27E−01	−8.70E−02	−4.27E−04

Total sigma = 0.30 for all frequencies.

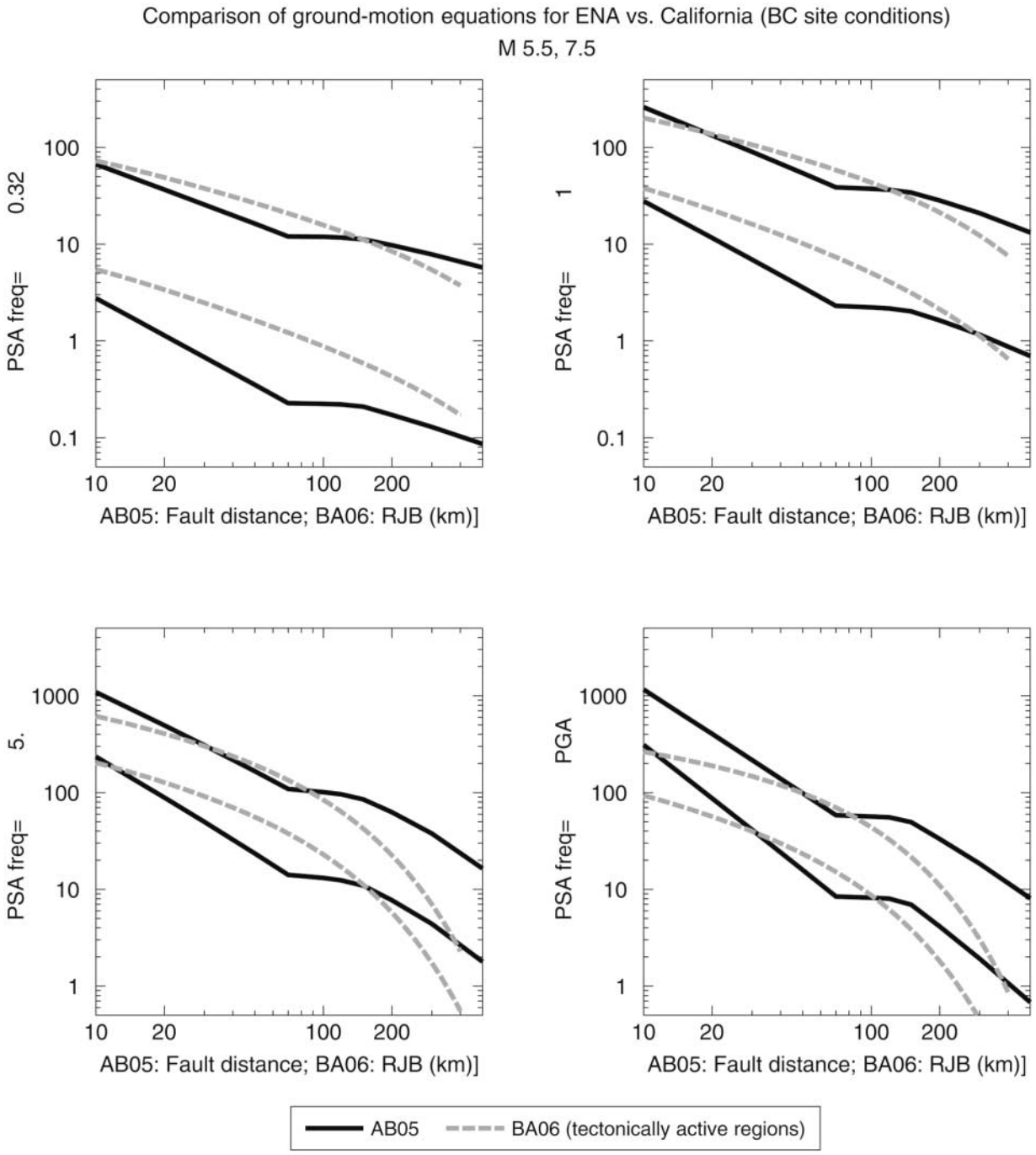

Figure 12. Comparison of the ground-motion prediction equations of this study for ENA for B/C boundary-site conditions, with those of Boore and Atkinson (2006) for active tectonic regions such as California.

Conclusion

Ground-motion prediction equations for rock and soil sites in ENA have been developed using a stochastic finite-fault methodology. Ground-motion predictions for hard-rock sites (NEHRP A, $V_{30} \geq 2000$ m/sec) in ENA may be made using equation (5) with the coefficients of Table 6 (hard-rock coefficients), setting $S = 0$. For any other site class, predictions should be made using equation (5) with the coefficients of Table 9 (NEHRP B/C boundary site class, $V_{30} = 760$ m/sec), with the frequency-dependent values for S as calculated according to equation (7a),(7b) with the coefficients of Table 8. The predictions are for our preferred median stress parameter of 140 bars. Alternative stress-parameter values may be modeled using the factors given in equation (6), with the coefficients of Table 7.

Acknowledgments

This work was financially supported by the U.S. Geological Survey National Earthquake Hazards Reduction Program (Grant 02HQGR0001), and by the U.S. Nuclear Regulatory Commission. We thank Chris Cramer and Ken Campbell for constructive reviews.

References

Abrahamson, N., and W. Silva (1997). Empirical response spectral attenuation relations for shallow crustal earthquakes, *Seism. Res. Lett.* **68,** 94–127.

Aki, K. (1967). Scaling law of seismic spectrum, *J. Geophys. Res.* **72,** 1217–1231.

Anderson, J., and S. Hough (1984). A model for the shape of the Fourier amplitude spectrum of acceleration at high frequencies, *Bull. Seism. Soc. Am.* **74,** 1969–1993.

Atkinson, G. (1993a). Source spectra for earthquakes in eastern North America, *Bull. Seism. Soc. Am.* **83,** 1778–1798.

Atkinson, G. (1993b). Notes on ground motion parameters for eastern North America: duration and H/V ratio, *Bull. Seism. Soc. Am.* **83,** 587–596.

Atkinson, G. (1996). The high-frequency shape of the source spectrum for earthquakes in eastern and western Canada, *Bull. Seism. Soc. Am.* **86,** 106–112.

Atkinson, G. (2004). Empirical attenuation of ground motion spectral amplitudes in southeastern Canada and the northeastern United States, *Bull. Seism. Soc. Am.* **94,** 1079–1095.

Atkinson, G., and D. Boore (1995). New ground motion relations for eastern North America, *Bull. Seism. Soc. Am.* **85,** 17–30.

Atkinson, G., and D. Boore (1997). Stochastic point-source modeling of ground motions in the Cascadia region, *Seism. Res. Lett.* **68,** 74–85.

Atkinson, G., and D. Boore (1998). Evaluation of models for earthquake source spectra in eastern North America, *Bull. Seism. Soc. Am.* **88,** 917–934.

Atkinson, G., and J. Cassidy (2000). Integrated use of seismograph and strong motion data to determine soil amplification in the Fraser Delta: results from the Duvall and George Strait earthquakes, *Bull. Seism. Soc. Am.* **90,** 1028–1040.

Atkinson, G., and S. Chen (1997). Regional seismograms from historical earthquakes in southeastern Canada, *Seism. Res. Lett.* **68,** 797–807.

Atkinson, G., and R. Mereu (1992). The shape of ground motion attenuation curves in southeastern Canada, *Bull. Seism. Soc. Am.* **82,** 2014–2031.

Atkinson, G., and W. Silva (1997). Empirical source spectra for California earthquakes, *Bull. Seism. Soc. Am.* **87,** 97–113.

Atkinson, G., and W. Silva (2000). Stochastic modeling of California ground motions, *Bull. Seism. Soc. Am.* **90,** 255–274.

Beresnev, I., and G. Atkinson (1997a). Modeling finite fault radiation from the ω^n spectrum, *Bull. Seism. Soc. Am.* **87,** 67–84.

Beresnev, I., and G. Atkinson (1997b). Shear wave velocity survey of seismographic sites in eastern Canada: Calibration of empirical regression method of estimating site response, *Seism. Res. Lett.* **68,** 981–987.

Beresnev, I., and G. Atkinson (1998a). Stochastic finite-fault modeling of ground motions from the 1994 Northridge, California earthquake, part I: Validation on rock sites, *Bull. Seism. Soc. Am.* **88,** 1392–1401.

Beresnev, I., and G. Atkinson (1998b). FINSIM—a FORTRAN program for simulating stochastic acceleration time histories from finite faults, *Seism. Res. Lett.* **69,** 27–32.

Beresnev, I., and G. Atkinson (2002). Source parameters of earthquakes in eastern and western North America based on finite-fault modeling, *Bull. Seism. Soc. Am.* **92,** 695–710.

Bodin, P., and S. Horton (2004). Source parameters and tectonic implications of aftershocks of the M_w 7.6 Bhuj earthquake of January 26, 2001, *Bull. Seism. Soc. Am.* **94,** 818–827.

Boore, D. (1983). Stochastic simulation of high-frequency ground motions based on seismological models of the radiated spectra, *Bull. Seism. Soc. Am.* **73,** 1865–1894.

Boore, D. (2003). Prediction of ground motion using the stochastic method, *Pure Appl. Geophys.* **160,** 635–676.

Boore, D. (2004). Can site response be predicted? *J. Earthquake Eng.* **8** (Special Issue 1), 1–41.

Boore, D., and G. Atkinson (1992). Source spectra for the 1988 Saguenay, Quebec earthquakes, *Bull. Seism. Soc. Am.* **82,** 683–719.

Boore, D., and G. Atkinson (2006). Boore-Atkinson NGA Empirical Ground Motion Model for the Average Horizontal Component of PGA, PGV and SA at Spectral Periods of 0.1, 0.2, 1, 2, and 3 Seconds, www.peer.berkeley.edu (last accessed June 2006).

Boore, D., and W. Joyner (1997). Site amplifications for generic rock sites, *Bull. Seism. Soc. Am.* **87,** 327–341.

Boore, D., W. Joyner, and T. Fumal (1997). Equations for estimating horizontal response spectra and peak acceleration from western North American earthquakes: a summary of recent work, *Seism. Res. Lett.* **68,** 128–153.

Brune, J. (1970). Tectonic stress and the spectra of seismic shear waves from earthquakes, *J. Geophys. Res.* **75,** 4997–5009.

Brune, J. (1971). Correction, *J. Geophys. Res.* **76,** 5002.

Choi, Y., and J. Stewart (2005). Nonlinear site amplification as a function of 30m shear wave velocity, *Earthquake Spectra* **21,** 1–30.

Cramer, C., and A. Kumar (2003). 2001 Bhuj, India earthquake engineering seismoscope recordings and eastern North America ground motion attenuation relations, *Bull. Seism. Soc. Am.* **93,** 1390–1394.

Electric Power Research Institute (EPRI) (1993). Guidelines for determining design basis ground motions, Early site permit demonstration program, Vol. 1, RP3302, Electric Power Research Institute, Palo Alto, California.

Electric Power Research Institute (EPRI) (2004). CEUS ground motion project final report. Technical Report 1009684. Electric Power Research Institute, Dominion Energy, Glen Allen, Virginia, Entergy Nuclear, Jackson, Mississippi; and Exelon Generation Company, Kennett Square, Pennsylvania, Palo Alto, California.

Frankel, A., C. Mueller, T. Barnhard, D. Perkins, E. Leyendecker, N. Dickman, S. Hanson, and M. Hopper (1996). National seismic hazard maps: documentation June 1996, *U.S. Geol. Surv. Open-File Rept. 96-532*, 69 pp.

Hanks, T., and R. McGuire (1981). The character of high-frequency strong ground motion, *Bull. Seism. Soc. Am.* **71,** 2071–2095.

Hartzell, S. (1978). Earthquake aftershocks as Green's functions, *Geophys. Res. Lett.* **5,** 1–14.

Heaton, T. (1990). Evidence for and implications of self-healing pulses of slip in earthquake rupture, *Phys. Earth Planet. Interiors* **64,** 1–20.

Heaton, T., and S. Hartzell (1986). Source characteristics of hypothetical subduction earthquakes in the Northwestern United States, *Bull. Seism. Soc. Am.* **76,** 675–708.

Hough, S., J. Armbruster, L. Seeber, and J. Hough (2000). On the Modified Mercalli Intensities and magnitudes of 1811–1812 New Madrid earthquakes, *J. Geophys. Res.* **105,** 839–864.

Irikura, K. (1983). Semi-empirical estimation of strong ground motions during large earthquakes, *Bull. Disaster Prevention Res. Inst., Kyoto Univ.* **33,** 63–104.

Johnston, A. (1996). Seismic moment assessment of earthquakes in stable continental regions. Part 3: The 1811–1812 New Madrid, 1886 Charleston, and 1755 Lisbon earthquakes, *Geophys. J. Int.* **126,** 314–344.

Joyner, W., and D. Boore (1986). On simulating large earthquakes by Green's-function addition of smaller earthquakes, in *Earthquake Source Mechanics, Maurice Ewing Series 6*, S. Das, *et al.* (Editors), Am. Geophys. Union, 269–274.

Lermo, J., and F. Chavez-Garcia (1993). Site effect evaluation using spectral ratios with only one station, *Bull. Seism. Soc. Am.* **83,** 1574–1594.

Ma, S., and G. Atkinson (2006). Focal depth distribution for earthquakes with MN $\geq$ 2.8 in western Quebec, southern Ontario and northern New York, *Bull. Seism. Soc. Am.* **96,** 609–623

Motazedian, D., and G. Atkinson (2005). Stochastic finite-fault model based on dynamic corner frequency, *Bull. Seism. Soc. Am.* **95,** 995–1010.

Sadigh, K., C. Chang, J. Egan, F. Makdisi, and R. Youngs (1997). Attenuation relationships for shallow crustal earthquakes based on California strong motion data, *Seism. Res. Lett.* **68,** 180–189.

Siddiqqi, J., and G. Atkinson (2002). Ground motion amplification at rock sites across Canada, as determined from the horizontal-to-vertical component ratio, *Bull. Seism. Soc. Am.* **92,** 877–884.

Singh, S., J. Pacheco, B. Bansal, X. Perez-Campos, R. Dattatrayam, and G. Suresh (2004). A source study of the Bhuj, India, earthquake of 26 January 2001 (M_w 7.6), *Bull. Seism. Soc. Am.* **94,** 1195–1206.

Somerville, P., N. Collins, N. Abrahamson, R. Graves, and C. Saikia (2001). Ground motion attenuation relations for the central and eastern United States, Report to U.S. Geological Survey, NEHRP External Research Program, Award No. 99-HQ-GR-0098.

Somerville, P., M. Sen, and B. Cohee (1991). Simulations of strong ground motions recorded during the 1985 Michoacan, Mexico and Valparaiso, Chile, earthquakes, *Bull. Seism. Soc. Am.* **81,** 1–27.

Toro, G., and R. McGuire (1987). Calculational procedures for seismic hazard analysis and its uncertainty in the eastern United States, in *Proc. Third Intl. Conf. Soil Dynamics and Earthquake Eng.*, Princeton, New Jersey, 195–206.

Toro, G., N. Abrahamson, and J. Schneider (1997). Model of strong ground motion in eastern and central North America: best estimates and uncertainties, *Seism. Res. Lett.* **68,** 41–57.

Tumarkin, A., and R. Archuleta (1994). Empirical ground motion prediction, *Ann. Geofis.* **37,** 1691–1720.

Wells, D., and K. Coppersmith (1994). New empirical relationships among magnitude, rupture length, rupture width, rupture area, and surface displacement, *Bull. Seism. Soc. Am.* **84,** 974–1002.

Zeng, Y., J. Anderson, and G. Yu (1994). A composite source model for computing realistic synthetic strong ground motions, *Geophys. Res. Lett.* **21,** 725–728.

Department of Earth Sciences
Carleton University
Ottawa, Ontario K1S 5B6, Canada
gmatkinson@aol.com
(G.M.A.)

U.S. Geological Survey
345 Middlefield Rd.
Menlo Park, California 94025
boore@usgs.gov
(D.M.B.)

Manuscript received 5 December 2005.